Norwegian University of
Science and Technology

Diffuse Small Angle X-Ray Scattering From Thin Film Structures In the Distorted Wave Born Approximation

Andreas Lønning Reiten

Nanotechnology
Submission date: July 2011
Supervisor: Dag Werner Breiby, IFY
Co-supervisor: Jostein Fløystad, IFY

Norwegian University of Science and Technology
Department of Physics

Diffuse Small Angle X-Ray Scattering From Thin Film Structures In the Distorted Wave Born Approximation

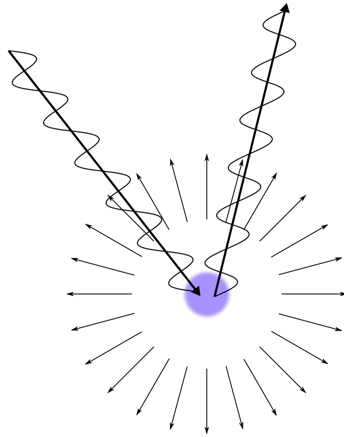

Andreas Lønning Reiten

July 8, 2011

Preface

This thesis is the result of a Master of Science in nanotechnology at the Norwegian University of Science and Technology (NTNU). The work has been carried out at the Department of Physics under supervision of Associate Professor Dag Werner Breiby and PhD candidate Jostein Bø Fløystad. The text targets readers with some background in experimental or theoretical X-ray physics who wish to improve their understanding of diffuse scattering from rough surfaces.

I would like to thank Post doc Kristin Høydalsvik at NTNU for providing suitable reference articles and for her consistent support. Ola Nilsen at the University of Oslo for thin film samples. Further, my thanks to the staff at Deutsches Elektronen-Synchrotron in Hamburg, Germany for providing synchrotron beamtime. I would also like to thank the rest of the X-ray research group for their helpfulness and positive attitudes.

Finally, I would like to express special thanks to my supervisor Dag W. Breiby and PhD candidate Jostein Bø Fløystad for their unwavering support and guidance throughout the project. I also thank my supervisor for the time and effort he has put into reading the thesis and the consecutive feedback he has given.

Abstract

The differential scattering cross section for diffuse scattering of X-rays from thin film structures is discussed within the framework of the distorted wave Born approximation (DWBA). In contrast to the standard Born approximation (BA), the distorted wave approach succeeds in calculating scattering from surfaces near the critical angle of reflection. The method is particularly useful for studying average surface properties.

Compromises made in the derivation of the model substantially simplify the final expression, but also limit its range of validity, which depends on the surface root mean square roughness σ and the momentum transfer between the incident and scattered X-rays perpendicular to the surface, Q_z. The approximation is valid so long as $Q_z\sigma \ll 1$. However, this is also the only regime where it is necessary to go beyond the simpler Born approximation.

A computer simulation software based on the DWBA is implemented in Python. The implemented DWBA depends on the fractal dimension of the surface features through a parameter h ($D = 3 - h$) and an in-plane correlation cut off length ζ. The various effects of changing key model parameters, among them ζ and h, is demonstrated. Comparison between experimental data and the DWBA model looks promising although there are some challenges in relation to determining the fractal dimension.

Finally, the feasibility of implementing the DWBA model in a multi-parameter fitting algorithm is discussed.

Contents

1 Introduction **1**

1.1 Motivation . . . 2

2 Thin Film X-ray Theory **4**

2.1 Snell's Law . . . 4

2.1.1 Index of Refraction for X-Rays . . . 6

2.2 Fresnel Equations . . . 7

2.3 Matrix Formalism for Multilayer Structures . . . 10

3 Scattering in the Distorted-Wave Born Approximation **13**

3.1 Gaussian Random Surfaces . . . 14

3.2 The Height-Height Correlation Function . . . 15

3.3 DWBA for Diffuse X-Ray Scattering From a Rough Surface . . . 17

3.4 Multiple Interfaces . . . 23

4 Experimental **26**

4.1 Samples . . . 26

4.2 Scan Methods . . . 27

4.3 W1 Beamline Characteristics . . . 28

5 Computer Simulation **33**

5.1 Model . . . 33

5.1.1 Computing Fourier Transform Integrals . . . 33

5.1.2 Fourier Integrals in the Model . . . 37

5.2 Implementation . . . 38

6 Results and Discussion **40**

6.1 Model - General Observations . . . 40

6.1.1 Small Angle Rocking Scan 40
6.1.2 Changing Model Parameters 42
6.1.2.1 Surface Roughness 42
6.1.2.2 Refractive Index 42
6.1.2.3 Hurst Exponent and Correlation Cut Off Length . 44
6.2 Comparison With Experiment 46
6.3 Outlook to Multi-parameter Fitting 54

7 Conclusion **55**

References **56**

Appendix **59**

A DWBA - General Expression **59**

B Fast Fourier Transform **63**

Chapter 1

Introduction

The first recorded use of reflectivity to characterize surfaces dates back to 1954 when Professor Lyman G. Parratt of Cornell University had an article published in Physical Review that presented X-ray studies of copper evaporated on glass [1]. Since then the technique has been extended to a wide range of both solid and liquid interfaces [2–4].

The wavelength of X-rays ($1 - 8$ Å) makes it feasible to study average features and properties of a sample at a comparable length scale within the irradiated volume, which is typically in the mm scale. In X-ray reflectivity a sample is struck by a narrow beam and the scattered signal is studied. The signal is built up of two components: the *specular* and the *diffuse*. The specularly scattered beam strictly obeys the law of reflection, i.e. that the incoming angle equals the outgoing. The diffuse signal comprises the scattering in all other directions and arises because of surface roughness. Most of the radiation is scattered in an approximate conical shape near the direction of the specular reflection.

Parratt's model, based on dispersion theory, only comprises the specular signal. However, in more recent years the *Born approximation*, based on quantum scattering theory, has been employed in reflectivity [5]. It successfully models both the specular and the diffuse components of the reflected signal, but breaks down at small angles of total reflection. It turns out that scattering in this regime can be modeled by the *distorted wave Born approximation*, which additionally takes into consideration a perturbation potential related to surface roughness [6,7].

The aim of this thesis is to study the distorted wave Born approximation to some detail. Specifically, the theory necessary to understand the model is presented in the first two chapters. Care is taken to highlight physical assumptions and mathematical approximations along the way. Then we look at some experimental considerations. The following chapter discusses a computer implementation of the model, in which there is emphasis on solving Fourier integrals, before we move on to look at how key model parameters affect the simulations. The model is then compared to experimental data, and finally there is a discussion regarding the possibility of using the model in a multi-parameter fitting algorithm to compare simulations with experimental data more efficiently.

Note that is this thesis, the term *reflectivity* is used to describe scattering from surfaces in general, and not just specular scattering.

With the exception of fig. 1.1, all figures are property of the author.

1.1 Motivation

Synchrotrons and linear accelerators around the world constitute an important part of modern-day materials science. They are huge facilities dedicated to the acceleration of charged particles that can be used to produce brilliant beams of X-rays and neutrons. The economic costs involved in the their construction and upkeep[1] leave little doubt about the impact of this type of research. Figure 1.1 shows the Swiss Light Source synchrotron (SLS) at the Paul Scherrer Institute in Switzerland.

Figure 1.1: The Swiss Light Source synchrotron at the Paul Scherrer Institute in Switzerland is a third-generation synchrotron light source. With an energy of 2.4 GeV, it provides photon beams of high brightness for research in materials science, biology and chemistry. The circular building in the upper picture is the actual synchrotron. Inside there is an electron storage ring, 288 m in circumference, that provides electromagnetic radiation to more than a dozen beamlines.

[1] The annual operating costs of the Swiss Light Source were estimated to 23 million Swiss Francs in 1999, on top of a total investment expenditure of 159 million Swiss Francs.

While many types of radiation can be used to probe materials, this thesis focuses on X-rays. When X-rays interact with matter, any given photon has a certain chance to be scattered by the electron cloud surrounding the atoms. The scattered radiation can be used to garner information about crystalline structure, grain sizes and preferred orientation to name a few examples. Moreover, X-ray reflectivity is a method that gives information about the thickness, roughness, and density of thin film structures when used together with appropriate theoretical models (i.e. computer simulations). Figure 1.2 shows an example of what experimental data may look like in the case of X-ray reflectivity. Specifically, the figure shows a small angle *rocking scan* of a 43 nm TiO_2 thin film on a Si substrate.

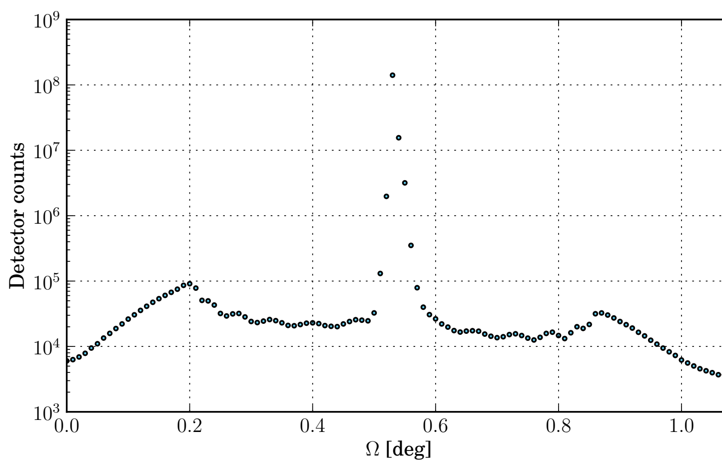

Figure 1.2: Small angle *rocking scan* of a 43 nm TiO_2 thin film on a Si substrate. The data was obtained in Hamburg, Germany, at Hamburger Synchrotronstrahlungslabor (HASYLAB) at Deutsches Elektronen-Synchrotron (DESY).

Chapter 2

Thin Film X-ray Theory

X-ray reflectivity is a powerful method for investigating surfaces and thin film structures. Typically, experimental data is compared to a computer model, and then the model parameters are adjusted until there is a close resemblance between the two. This chapter gives an introduction to the physics behind X-ray reflectivity.

2.1 Snell's Law

Snell's law [8] states that when an electromagnetic wave passes through an interface between two media of different refractive indices, n_0 and n_1, the following relation is fulfilled:

$$\frac{\sin\theta_0}{\sin\theta_1} = \frac{n_1}{n_0} = \frac{v_0}{v_1}, \tag{2.1}$$

where θ_0 and θ_1 are the angles between the normal to the interface and the wave in each media as shown in fig. 2.1, and v_0 and v_1 are the phase speeds of the waves. This has implications for reflectivity because the fraction of light that is reflected by the surface depends on these two angles.

An electromagnetic wave is associated with a wave vector, $\mathbf{k}$, which is related to the wavelength λ by

$$\mathbf{k} = \frac{2\pi}{\lambda}\widehat{\mathbf{k}}, \tag{2.2}$$

where $\widehat{\mathbf{k}}$ is a unit vector in the direction of propagation. In this text the components of $\mathbf{k}$ are denoted by k_x, k_y, and k_z, where z is normal to the sample surface and k_x is the projection of $\mathbf{k}$ on the surface, cf. fig. 2.2. Figure 2.2 also shows the momentum transfer vector, denoted by $\mathbf{Q}$. In the illustrated case $\mathbf{Q} = \mathbf{k_1} - \mathbf{k_0}$ is the momentum transfer between the incoming and outgoing (reflected) wave. Note that the magnitude of $\mathbf{k_x}$ is constant and independent of changes in the refractive

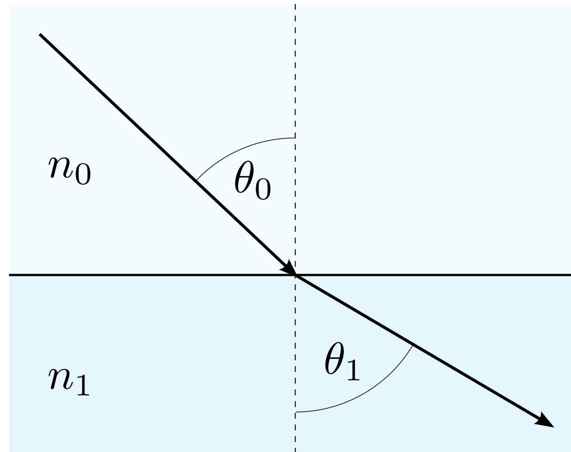

Figure 2.1: When an electromagnetic wave passes through an interface between two media of different refractive indices, n_0 and n_1, it changes direction. The process is described mathematically by Snell's law, cf. eq. (2.1).

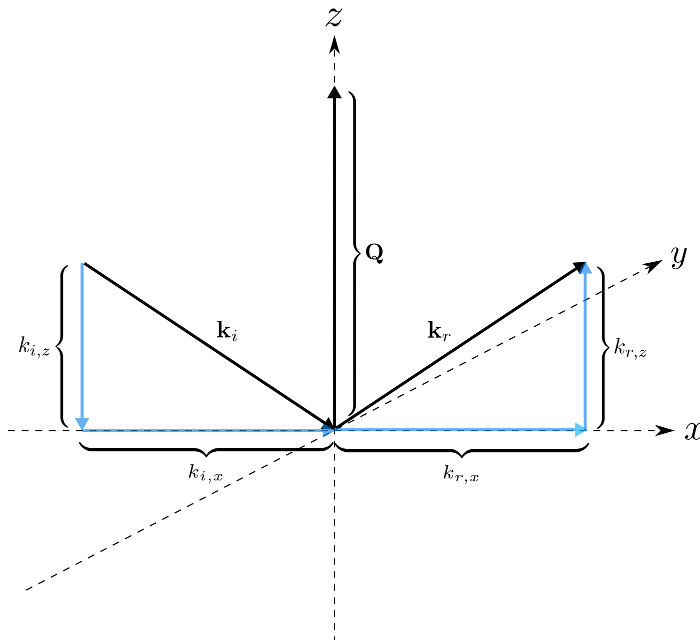

Figure 2.2: The wave vectors of an incoming and reflected wave, denoted $\mathbf{k}_i$ and $\mathbf{k}_r$, with respect to a surface in the (x, y)-plane. $\mathbf{Q} = \mathbf{k_1} - \mathbf{k_0}$ is the momentum transfer vector.

index. This can be shown using the well known Planck-Einstein equation [9],

$$E = \hbar\omega, \tag{2.3}$$

which gives the relation between the energy E and frequency ω of a photon. Under the assumption that the energy of the photon is conserved over the transition into a new media and the relation $\omega = 2\pi v/\lambda$, we can write

$$\frac{k_1}{k_0} = \frac{v_0}{v_1} = \frac{n_1}{n_0}, \tag{2.4}$$

where k_0 and k_1 are the magnitudes of the incoming and outgoing wave vectors in the media characterized by n_0 and n_1, respectively. By plugging this equation into Snell's law it should be clear that

$$k_{0,x} = k_{1,x}. \tag{2.5}$$

Substituting for $k_1 = \sqrt{k_{1,x}^2 + k_{1,z}^2}$ in eq. (2.4) and using the result of eq. (2.5) yields

$$k_{z,1} = -\sqrt{k_0^2 \frac{n_1}{n_0}^2 - k_x}. \tag{2.6}$$

Furthermore, if $n_0 = 1.0$ for the topmost medium (air or vacuum), it can be shown that

$$k_{z,j} = -\sqrt{k_0^2 n_j^2 - k_x}, \tag{2.7}$$

where j is the index of any subjacent layer. This is an essential relation in calculating the reflectivity from multilayer structures.

2.1.1 Index of Refraction for X-Rays

The index of refraction is a measure of the speed of light in a given medium. Specifically, the parameter can be written as

$$n = \frac{c}{v}, \tag{2.8}$$

where c is the speed of light in vacuum, and v is the phase speed of the light in the medium. n depends on the wavelength of the radiation in question, and in the case of X-rays, v is actually greater than c, meaning that n is below unity. In this case it is common to express the refractive index as

$$n = 1 - \delta + i\beta. \tag{2.9}$$

The imaginary part β is related absorption and leads to a reduction in the radiation intensity with increasing distance traveled in the medium. Specifically, the reduction in intensity I is given by

$$I = I_0 e^{-\alpha s}, \tag{2.10}$$

where s is the distance traveled in the medium, and α is the *absorption coefficient* given by

$$\alpha = \frac{4\pi\beta}{\lambda}. \tag{2.11}$$

A thorough description of refractive indices is given in [8].

Since the refractive index is slightly less than one, a beam incident on a flat interface can be totally reflected if the angle between the surface and the incident beam is less than a certain critical angle α_c, which is approximately equal to $\sqrt{2\delta}$. When $n_0 > n_1$, cf. fig. 2.1, this phenomena is called total *internal* reflection. If $n_0 < n_1$, it is called total *external* reflection.

2.2 Fresnel Equations

The Fresnel equations give relations between the reflected, transmitted, and incident amplitudes of an electromagnetic wave as it passes through an interface between two media of different refractive indices. Figure 2.3 shows a ray of light incident on an interface between two media of refractive indices n_0 and n_1. Part of the beam is transmitted, and the remainder is reflected back. The depicted wave is polarized in the *transverse electric* mode (TE) in which the electric component is parallel to the interface (*s-polarization*). It is assumed that any incident wave exhibits this kind of polarization. Note that X-ray synchrotrons predominantly emit horizontally (TE) polarized radiation.

Maxwell's equations impose boundary conditions on the incident, transmitted, and reflected wave. Their electric components are denoted by

$$\mathbf{E}_i = E_i e^{i\mathbf{k}_i \cdot \mathbf{r}} \widehat{\mathbf{y}} \tag{2.12a}$$

$$\mathbf{E}_t = E_t e^{i\mathbf{k}_t \cdot \mathbf{r}} \widehat{\mathbf{y}} \tag{2.12b}$$

$$\mathbf{E}_r = E_r e^{i\mathbf{k}_r \cdot \mathbf{r}} \widehat{\mathbf{y}}, \tag{2.12c}$$

respectively. The factor $e^{\omega t}$ has been neglected as the frequency of each wave is the same assuming the energy is conserved. Faraday's law [10] states that,

$$\oint_C \mathbf{E} \cdot \mathrm{d}\mathbf{l} = -\frac{\partial}{\partial t} \int_S \mathbf{B} \cdot \mathrm{d}\mathbf{S}, \tag{2.13}$$

where $\mathrm{d}\mathbf{l}$ is an infinitesimal line segment of the closed contour C bounding the area S, cf. fig. 2.4. Thus we can write

$$(\mathbf{l}_0 + \mathbf{l}_1 + \mathbf{l}_2 + \mathbf{l}_3) \cdot (\mathbf{E}_0 + \mathbf{E}_1) = -\frac{\partial}{\partial t} \int_S \mathbf{B} \cdot \mathrm{d}\mathbf{S} = 0, \tag{2.14}$$

which leads to the general conclusion that in the limit $\mathbf{l}_0 = \mathbf{l}_2 \to 0$ where $S \to 0$

$$E_{0,tangential} = E_{1,tangential}, \tag{2.15}$$

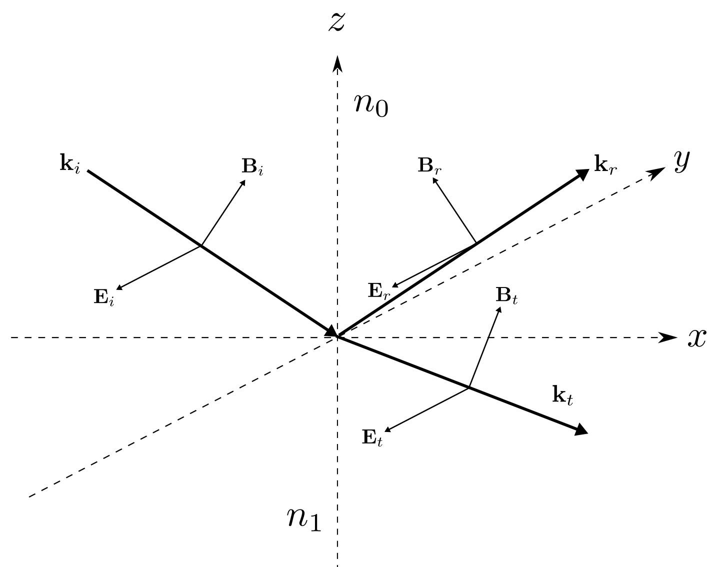

Figure 2.3: A wave vector $\mathbf{k}_i$ (i.e. electromagnetic wave) incident on an interface between two media of refractive indices n_0 and n_1. Part of the wave is transmitted ($\mathbf{k}_t$), and the remainder is reflected back ($\mathbf{k}_r$). The depicted wave is polarized in the transverse electric mode in which the electric component is tangential to the interface.

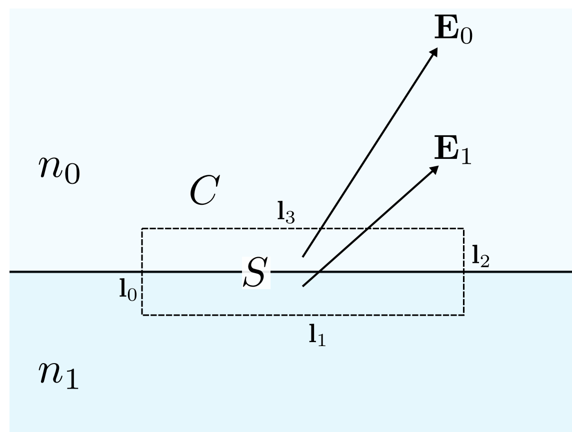

Figure 2.4: The rectangular closed contour C spanning over an interface between two media of different refractive indices, n_0 and n_1. Note that S is the area *within the contour*.

where $E_{0,tangential}$ and $E_{1,tangential}$ are the tangential components of the electric field right above and below the boundary. Consequently, the tangential component of the electric field is continuous at the boundary, meaning that

$$E_i + E_r = E_t, \tag{2.16}$$

where $\mathbf{r}$ has been set equal to zero at the boundary (cf. eqs. (2.12a) to (2.12c)).

The magnetic components, given by

$$\mathbf{B}_i = (B_i \cos\theta_i \hat{\mathbf{x}} - B_i \sin\theta_i \hat{\mathbf{z}})\, e^{i\mathbf{k}_i \cdot \mathbf{r}} \tag{2.17a}$$

$$\mathbf{B}_t = (B_t \cos\theta_t \hat{\mathbf{x}} - B_t \sin\theta_t \hat{\mathbf{z}})\, e^{i\mathbf{k}_t \cdot \mathbf{r}} \tag{2.17b}$$

$$\mathbf{B}_r = (-B_r \cos\theta_r \hat{\mathbf{x}} - B_r \sin\theta_r \hat{\mathbf{z}})\, e^{i\mathbf{k}_r \cdot \mathbf{r}}, \tag{2.17c}$$

obey the law of conservation of magnetic flux [10],

$$\oint_S \mathbf{B} \cdot d\mathbf{S} = 0, \tag{2.18}$$

where $d\mathbf{S}$ is an infinitesimal part of the surface S with surface nomral $\mathbf{S}$. Consequently, with S superimposed on the boundary,

$$\mathbf{B}_0 \cdot \mathbf{S} = \mathbf{B}_1 \cdot \mathbf{S}, \tag{2.19}$$

which gives

$$B_{0,normal} = B_{1,normal}, \tag{2.20}$$

where $B_{0,normal}$ and $B_{1,normal}$ are the components of the magnetic field normal to the boundary on each side of the interface. Equation (2.20) can also be re-expressed using the tangential components of the magnetic field. It then yields

$$\frac{B_{0,tangential}}{\mu_0} = \frac{B_{1,tangential}}{\mu_1}, \tag{2.21}$$

where μ_0 and μ_1 are the magnetic permeabilities on the two sides of the interface. Applying this result to the system in fig. 2.3 yields

$$\frac{B_i}{\mu_0}\cos\theta_i - \frac{B_r}{\mu_0}\cos\theta_i = \frac{B_t}{\mu_1}\cos\theta_t, \tag{2.22}$$

which can be simplified using the common occurrence that $\mu_0 \approx \mu_1 \approx \mu_{vacuum}$ [11]. Combining eqs. (2.16) and (2.22) and the relation between magnetic and electric fields, $E = vB = cB/n$, where c is the speed of light in vacuum and $n = n_1/n_0$, the reflection and transmission amplitude coefficients for TE polarization become

$$r_{TE} = \frac{E_r}{E_i} = \frac{\cos\theta_i - n\cos\theta_t}{\cos\theta_i + n\cos\theta_t} \tag{2.23a}$$

$$t_{TE} = \frac{E_t}{E_i} = \frac{2\cos\theta_i}{\cos\theta_i + n\cos\theta_t}. \tag{2.23b}$$

r_{TE} and t_{TE} for a Si substrate is shown in fig. 2.5.

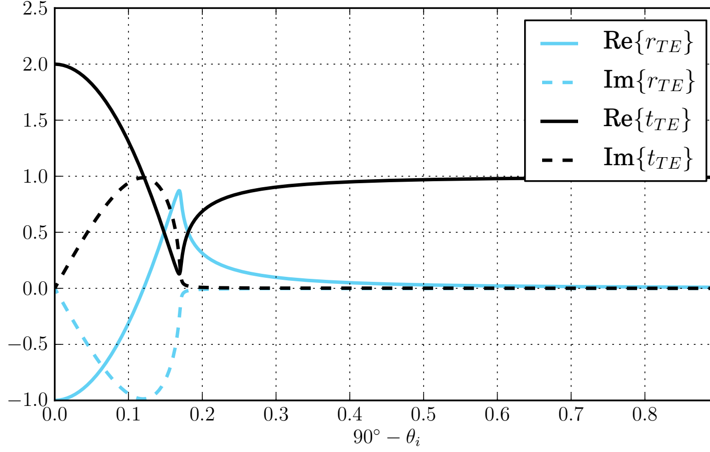

Figure 2.5: The reflection and transmission amplitude coefficients for a Si substrate at small angles between the surface and the incident beam. The wavelength $\lambda = 1.1808$ Å $\delta = 4.43 \times 10^{-6}$ and $\beta = 6.06 \times 10^{-8}$. The critical angle is $\sqrt{2\delta} \approx 0.17\,°$.

2.3 Matrix Formalism for Multilayer Structures

In the case of multilayer structures the incoming X-rays are multiply reflected by several interfaces, and the reflected amplitude, E_r, ends up with contributions from each interface. The Fresnel equations derived in the previous section assumed *one* interface (i.e. air and a substrate). In this section the equations are reworked to be valid also for multilayer structures with several interfaces.

We introduce a multilayer-friendly notation for the electrical and magnetic fields, cf. fig. 2.6. Assuming TE polarization, continuity of the electrical field yields

$$E_j^- e^{\mathbf{k}_j^- \cdot \mathbf{r}} + E_j^+ e^{\mathbf{k}_j^+ \cdot \mathbf{r}} = E_{j+1}^- e^{\mathbf{k}_{j+1}^- \cdot \mathbf{r}} + E_{j+1}^+ e^{\mathbf{k}_{j+1}^+ \cdot \mathbf{r}}. \tag{2.24}$$

Since the model now extends over multiple interfaces, we no longer assume $\mathbf{r} = 0$. Equation (2.24) can be simplified to yield

$$E_j^- e^{k_{j,z}^- z} + E_j^+ e^{-k_{j,z}^- z} = E_{j+1}^- e^{k_{j+1,z}^- z} + E_{j+1}^+ e^{-k_{j+1,z}^- z}. \tag{2.25}$$

Similarly, continuity of the magnetic field gives

$$B_j^- \cos\theta_i e^{k_{j,z}^- z} + B_j^+ \cos\theta_i e^{-k_{j,z}^- z} = B_{j+1}^- \cos\theta_t e^{k_{j+1,z}^- z} + B_{j+1}^+ \cos\theta_t e^{-k_{j+1,z}^- z}. \tag{2.26}$$

By combining eqs. (2.25) and (2.26) and for simplicity writing $k_{j,z}^- = k_{j,z}$ and

$k^{-}_{j+1,z} = k_{j+1,z}$ it can be shown that

$$E^{-}_{j} = \frac{1}{2}\left(E^{-}_{j+1}\frac{k_{j+1,z}+k_{j,z}}{k_{j,z}}e^{-i(k_{j+1,z}-k_{j,z})z} + E^{+}_{j+1}\frac{k_{j+1,z}-k_{j,z}}{k_{j,z}}e^{i(k_{j+1,z}+k_{j,z})z}\right) \tag{2.27a}$$

$$E^{+}_{j} = \frac{1}{2}\left(E^{-}_{j+1}\frac{k_{j+1,z}-k_{j,z}}{k_{j,z}}e^{-i(k_{j+1,z}+k_{j,z})z} + E^{+}_{j+1}\frac{k_{j+1,z}+k_{j,z}}{k_{j,z}}e^{i(k_{j+1,z}-k_{j,z})z}\right), \tag{2.27b}$$

or, expressed as matrices,

$$\begin{bmatrix} E^{-}_{j} \\ E^{+}_{j} \end{bmatrix} = \begin{bmatrix} m_{11} & m_{12} \\ m_{21} & m_{22} \end{bmatrix} \begin{bmatrix} E^{-}_{j+1} \\ E^{+}_{j+1} \end{bmatrix} \tag{2.28}$$

where

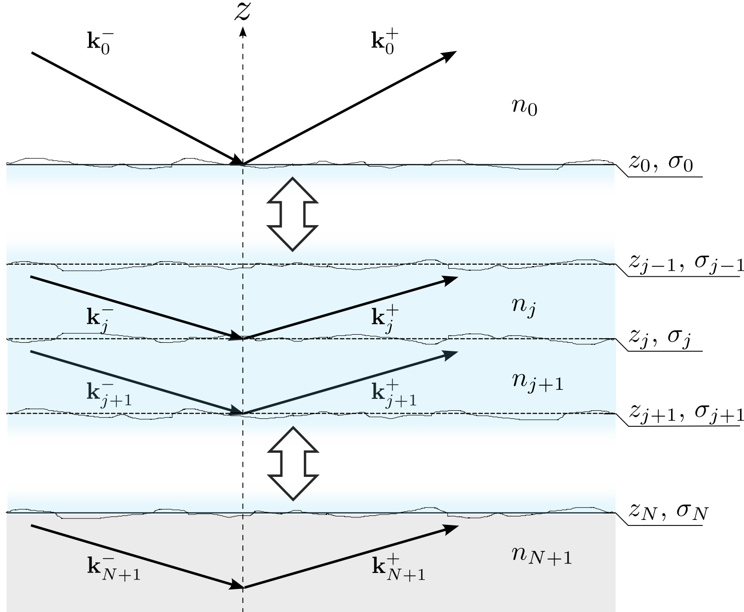

Figure 2.6: The multilayer approach requires an extra wave vector ($\mathbf{k}^{+}_{j+1}$) per interface in addition to those associated with the incident ($\mathbf{k}^{-}_{j}$), transmitted ($\mathbf{k}^{-}_{j+1}$), and reflected ($\mathbf{k}^{+}_{j}$) waves. It corresponds to the reflected amplitude from subjacent layers. j denotes the medium index, and $+$ and $-$ correspond to incoming and outgoing waves, respectively. n_j, σ_j, and z_j refer to the refractive index, surface roughness, and depth of each layer.

$$\begin{aligned}
m_{11} &= \frac{k_{j+1,z} + k_{j,z}}{2k_{j,z}} e^{-i(k_{j+1,z}-k_{j,z})z} \\
m_{12} &= \frac{k_{j+1,z} - k_{j,z}}{2k_{j,z}} e^{i(k_{j+1,z}+k_{j,z})z} \\
m_{11} &= \frac{k_{j+1,z} - k_{j,z}}{2k_{j,z}} e^{-i(k_{j+1,z}+k_{j,z})z} \\
m_{12} &= \frac{k_{j+1,z} + k_{j,z}}{2k_{j,z}} e^{i(k_{j+1,z}-k_{j,z})z}.
\end{aligned} \tag{2.29}$$

This is known as the matrix formalism, and it gives the stacking reflected and transmitted amplitudes for each layer. For example, a structure containing N layers requires $N+1$ matrices like eq. (2.28)[1]. For the substrate it is common practice to set $E^-_{N+1} = 1$ and $E^+_{N+1} = 0$ to close the system of equations. This is valid assuming the part of the beam that enters the substrate is not reflected. The formalism can also be used to model a graded interface by using an arbitrary number of slices, as opposed to simply separating layer-by-layer.

Reflection and transmission amplitude coefficients for the j'th layer are

$$r_{TE} = \frac{E^+_j}{E^-_j} \tag{2.30a}$$

$$t_{TE} = \frac{E^-_{j+1}}{E^-_j}. \tag{2.30b}$$

Equation (2.7) is used to calculate all the instances of $k_{j,z}$ that are required.

The above discussion looked at scattering from perfectly flat surfaces. For rough surfaces, it is found that [12] eq. (2.28) becomes

$$\begin{bmatrix} E^-_j \\ E^+_j \end{bmatrix} = \begin{bmatrix} m_{11} e^{-(k_{j+1,z}-k_{j,z})^2 \frac{\sigma_j^2}{2}} & m_{12} e^{-(k_{j+1,z}+k_{j,z})^2 \frac{\sigma_j^2}{2}} \\ m_{21} e^{-(k_{j+1,z}+k_{j,z})^2 \frac{\sigma_j^2}{2}} & m_{22} e^{-(k_{j+1,z}-k_{j,z})^2 \frac{\sigma_j^2}{2}} \end{bmatrix} \begin{bmatrix} E^-_{j+1} \\ E^+_{j+1} \end{bmatrix} \tag{2.31}$$

where σ_j is the root mean square (r.m.s.) roughness of the j'th interface as shown in fig. 2.6. $\sigma > 0$ leads to a decrease of the reflection and transmission amplitude coefficients due to non-specular scattering which is discussed in the next chapter.

[1] A simple air-substrate model has no "layers".

Chapter 3

Scattering in the Distorted-Wave Born Approximation

When an X-ray strikes a perfectly flat surface, the only measurable reflected signal goes out at an angle that fulfills the law of reflection, i.e. $\theta_i = \theta_r$. This is called specular reflection. However, most real-world samples exhibit some surface roughness such that a portion of the incoming beam is reflected in other directions depending on the underlying texture. Surface roughness gives rise to an off-specular (diffuse) component to the reflected signal.

The intensity of the specular reflection can be calculated as the square norm of the reflection amplitude coefficient, which in turn is found through eq. (2.31). While measuring the specular reflectivity as a function of incident angle is sufficient to find the surface and interface roughness parameters σ_j, it does not give any information about the in-plane correlation length, which is the length over which rough features are correlated, or the fractal dimension of the surface. However, the diffuse signal does contain such information. The distorted-wave Born approximation (DWBA) gives a reasonably precise model for diffuse scattering near the critical angle while keeping the computational complexity low enough for practical use. Well above the critical angle the Born approximation (BA) is commonly employed as the added complexity of the DWBA is not necessary. Both models share the same origin in quantum scattering theory.

This chapter presents an expression of the DWBA for use in X-ray thin film studies. Specifically, the differential scattering cross section is found for diffuse scattering from a substrate, and then for thin films and multilayer structures. In preparation for this, the chapter begins with a description of the average properties of rough surfaces.

A presentation of the general expression for the BA and the DWBA can be found in appendix A.

3.1 Gaussian Random Surfaces

The average properties of a surface, which is to be investigated, are based on analysis of X-rays that originate from a finite size area. The area, which corresponds to the area illuminated by the incoming beam, covers a large number of microscopic formations and structures that are more or less correlated. The surface roughness can resemble patterns, or have a fractal structure. This section briefly shows how such surfaces can be described mathematically.

The rough surface of a substrate, given by $z(x,y)$, can be described by a height distribution function $\omega(z)$ where the average surface height ($z=0$) is chosen such that

$$\int_0^\infty \omega\left(z\right)\ \mathrm{d}z = \int_{-\infty}^0 \omega\left(z\right)\ \mathrm{d}z = \frac{1}{2}. \tag{3.1}$$

The function $\omega(z)$ gives the probability distribution of the various heights across the surface. A common assumption in the derivation of the DWBA for X-ray scattering is that the rough surface is taken to be a *Gaussian random surface*, meaning that

$$\omega\left(z\right) = \frac{e^{-z^2/2\sigma^2}}{\sigma\sqrt{2\pi}}, \tag{3.2}$$

where σ is the r.m.s. roughness.

In the coming derivation of the DWBA, it is at one point necessary to take a configurational average in the z-direction of the form $\langle \exp\left\{i[sz(x,y) - s'z(x',y')]\right\}\rangle$, where s is a complex variable. As $[sz(x,y) - s'z(x',y')]$ is a Gaussian random variable (under the assumption of a Gaussian random surface), this configurational average yields [6]

$$\left\langle e^{i[sz(x,y)-s'z(x',y')]}\right\rangle = e^{-\mathrm{g}(x,y)/2}, \tag{3.3}$$

where

$$\begin{aligned}\mathrm{g}(x,y) &= \left\langle [sz(x,y) - s'z(x',y')]^2 \right\rangle \\ &= s^2\left\langle z^2(x,y)\right\rangle + s'^2\left\langle z^2(x',y')\right\rangle - ss'\left\langle z(x,y)z(x',y')\right\rangle \\ &= s^2\sigma^2 + s'^2\sigma^2 - ss'C(x-x',y-y').\end{aligned} \tag{3.4}$$

Here, $C(x-x',y-y')$ is a height-height correlation function describing to what degree the heights at coordinates (x',y') and (x,y) are correlated. The choice of $C(x-x',y-y')$ is crucial, and a suitable form is described in section 3.2.

3.2 The Height-Height Correlation Function

The height-height correlation function describes to what degree two heights $z(x', y')$ and $z(x, y)$ on a surface are correlated. Denoting the relative coordinates $X = x' - x$ and $Y = y' - y$, Sinha et al. suggested that the function $C(X, Y)$ be expressed as

$$C(X,Y) = \sigma^2 e^{-\left(\frac{\sqrt{X^2+Y^2}}{\zeta}\right)^{2h}}, \tag{3.5}$$

where ζ is a finite cut off length describing the correlation length of the surface features, and h, called the *Hurst exponent*, specifies the fractal dimension of the surface by $D = 3 - h$. A perfectly smooth surface has two dimensions, so $0 \leq h \leq 1$. If h is small, the fractal dimension is high and the surface has relatively "protruding" features (jagged surface), cf fig. 3.1. Note that eq. (3.5) is symmetric

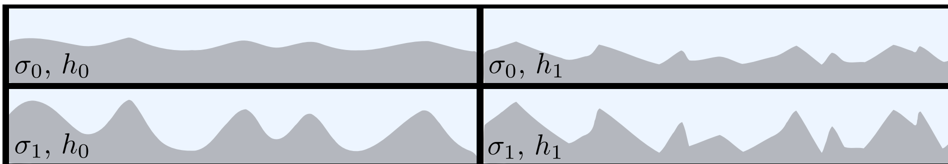

Figure 3.1: The Hurst exponent h determines the fractal dimension of a rough surface through $D = 3 - h$. The figure shows surfaces with two different Hurst exponents $h_0 > h_1$ and root mean square roughnesses $\sigma_0 < \sigma_1$. Smaller h results in a more jagged surface.

in $R = \sqrt{X^2 + Y^2}$, or $r = \sqrt{x^2 + y^2}$ by defining that $x' = y' \equiv 0$ such that $X = -x$ and $Y = -y$.

Figures 3.2 and 3.3 demonstrate the shape of eq. (3.5) as a function of $r = \sqrt{x^2 + y^2}$ for various values of the parameters h and ζ. In practice, ζ must be smaller than the coherence length of the beam in order for the the theory presented in this chapter to match experimental results. The coherence length is the spatial length (transverse and longitudinal) over which the X-rays are in phase (remember that the incoming beam has a cross section of approx. $1\,\text{mm}^2$). In this instance it is the coherence length parallel to the sample surface that is of interest. The significance is that interference will be strong within the coherence volume, but not beyond it. Consequently, the coherence length of the beam restricts the *maximum* length scales of the roughness characteristics that can be studied.

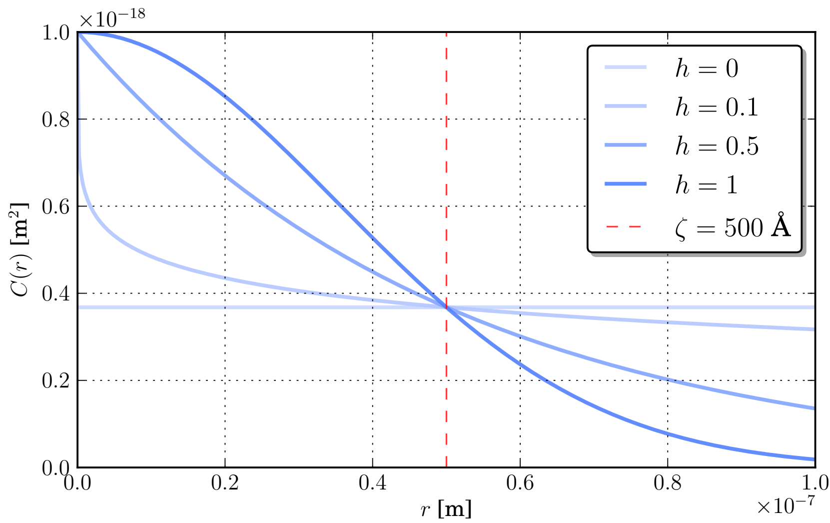

Figure 3.2: The correlation function $C(r)$ for various values of the Hurst exponent h. The cut off parameter ζ is indicated by the dotted red line.

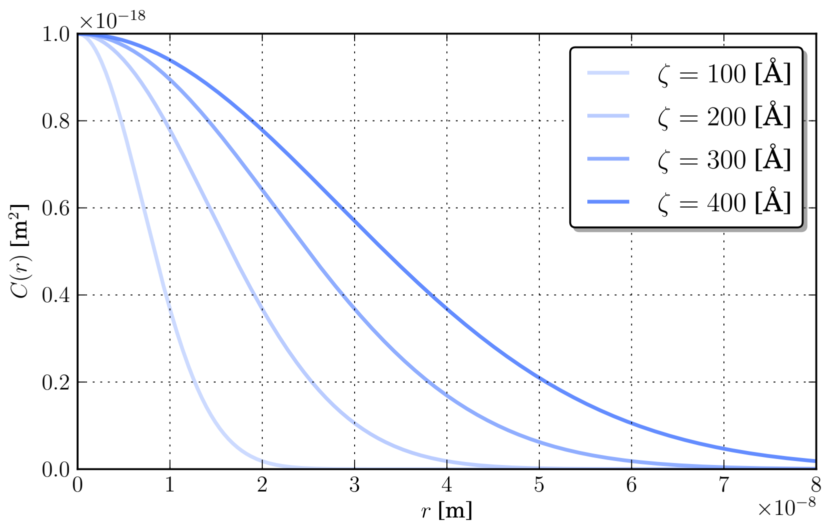

Figure 3.3: The correlation function $C(r)$ for various values of the cut off parameter ζ. $h = 1$.

3.3 DWBA for Diffuse X-Ray Scattering From a Rough Surface

The DWBA states that the probability amplitude for a particle or photon to go from one state to another in the presence of an exactly solvable potential plus a small perturbation potential is given by

$$\boxed{\langle 1|\, T\, |0\rangle = \langle \psi_1|\, V_0\, |\phi_0\rangle + \langle \psi_1|\, V_1\, |\psi_0\rangle} \tag{3.6}$$

which follows[1] from eq. (A.19). In this section the DWBA is used to describe diffuse scattering of grazing incidence X-rays on rough surfaces. The presentation closely follows and complements the article *X-ray and neutron scattering from rough surfaces* published in 1988 by Sinha et al. [6]. That article also includes expressions for specular scattering.

The starting point of the derivation is a set of wave functions and potentials to describe the system in which scattering occurs. A plane wave from an X-ray source describes the incoming X-rays prior to scattering:

$$\phi_0 = Ce^{i\mathbf{k}_{0,i}\cdot\mathbf{r}}, \tag{3.7}$$

where C is a normalization constant. Upon striking a potential (i.e. a surface or interface), the wave function evolves into

$$\psi_0 = \begin{cases} C[e^{i\mathbf{k}_{0,i}\cdot\mathbf{r}} + r_0 e^{i\mathbf{k}_{0,r}\cdot\mathbf{r}}] & \text{for } z > 0 \\ Ct_0 e^{i\mathbf{k}_{0,t}\cdot\mathbf{r}} & \text{for } z < 0 \end{cases} \tag{3.8}$$

which from here on will be referred to as the *source wave*. The components correspond to an incident, a reflected, and a transmitted wave. r_0 and t_0 are Fresnel amplitude coefficients, cf. section 2.2.

The DWBA requires a third wave function to describe the diffusively scattered X-rays, given by

$$\psi_1 = \begin{cases} C[e^{i\mathbf{k}^*_{1,i}\cdot\mathbf{r}} + r^*_1 e^{i\mathbf{k}^*_{1,r}\cdot\mathbf{r}}] & \text{for } z > 0 \\ Ct^*_1 e^{i\mathbf{k}^*_{1,t}\cdot\mathbf{r}} & \text{for } z < 0 \end{cases} \tag{3.9}$$

It is referred to as the *detector wave* as it defines the outgoing direction in which scattering will later be calculated, just like a detector in an experimental setup. Figure 3.4 illustrates the concept of a source wave and a detector wave.

A key property of the DWBA is that it relies on two potentials; one describing the unperturbed system, and another corresponding to a small perturbation. In X-ray scattering the potential of the unperturbed system describes a perfectly flat surface, given by

$$V_0 = \begin{cases} k_0^2\left(1 - n^2\right) & \text{for } -\infty < z < 0 \\ 0 & \text{for } z > 0 \end{cases} \tag{3.10}$$

[1] The approximation in the DWBA consisted of letting ψ_0 describe scattering due *only* to V_0, as opposed to V_0 *and* the perturbation potential V_1. In effect, the Schrödinger equation describing ψ_0 has been approximated to only include one of two potentials, namely V_0. On a side note, ψ_1 also depends only on V_0, but this is not an approximation.

The perturbation potential V_1 corresponds to a deviation from the perfectly flat surface and incorporates surface roughness in the model. It is given by

$$V_1 = \begin{cases} k_0^2\left(1-n^2\right) & \text{for } 0<z<z\left(x,y\right) \text{ if } z\left(x,y\right)>0 \\ -k_0^2\left(1-n^2\right) & \text{for } 0>z>z\left(x,y\right) \text{ if } z\left(x,y\right)<0 \\ 0 & \text{elsewhere} \end{cases} \tag{3.11}$$

where $z(x,y)$ describes the topography of a rough surface. The perturbation potential is confined to the volume bounded by $z(x,y)$ and a plane at $z=0$. The form of the given potential functions are commonly used in X-ray reflectivity theory, and a thorough description can be found in [13]. The differential scattering

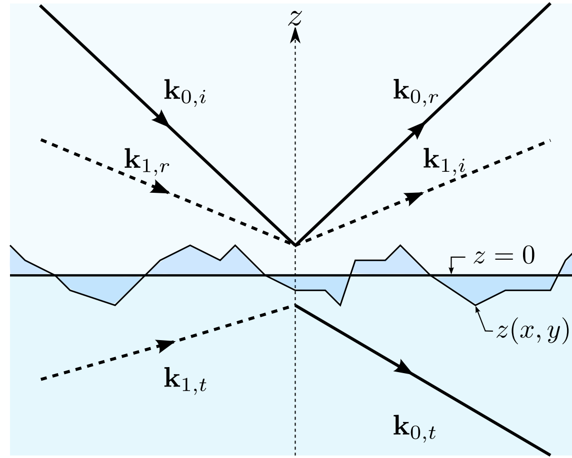

Figure 3.4: The source wave ψ_0 and detector wave ψ_1 in the DWBA. The perturbation potential V_1 is limited to the volume bounded by $z=0$ and the function $z(x,y)$ describing the topography of the rough surface.

cross section follows from eq. (A.14) and yields for X-rays

$$\boxed{\frac{\mathrm{d}\sigma}{\mathrm{d}\Omega}=\frac{\left|\langle 1|\,T\,|0\rangle\right|^2}{16\pi^2\left|C\right|^4}=\frac{\left|\langle\psi_1|\,V_0\,|\phi_0\rangle+\langle\psi_1|\,V_1\,|\psi_0\rangle\right|^2}{16\pi^2\left|C\right|^4}} \tag{3.12}$$

It describes the probability of finding a scattered particle within a given solid angle.

Retreating for a moment from the notation above, consider the fact that the numerator in eq. (3.12) is an expression of the type

$$\left|A+B\right|^2.$$

B is a spatially fluctuating quantity because of its dependence on $z\left(x,y\right)$ through V_1, and it is therefore necessary to take the configurational average, which is given

by

$$\left\langle |A+B|^2 \right\rangle = \underbrace{|A+\langle B\rangle|^2}_{\text{spec}} + \underbrace{\langle BB^*\rangle - \langle B\rangle \langle B\rangle^*}_{\text{diff}}, \tag{3.13}$$

where the bra-ket notation and configurational average are not to be confused. The first term corresponds to scattering in the specular direction, and the last two terms constitute the variance of B and correspond to the diffuse signal. Note that if the perturbation potential is zero ($V_1 = 0$), then $B = 0$ and eq. (3.13) becomes simply $|A|^2$. However, for a finite perturbation potential it is necessary to calculate the quantities $\langle B\rangle$ and $\langle BB^*\rangle$. The strategy is therefore to calculate B, $\langle B\rangle$, and $\langle BB^*\rangle$ to find an expression for the diffuse signal, given by

$$\left(\frac{\mathrm{d}\sigma}{\mathrm{d}\Omega}\right)_{\text{diff}} = \frac{\left|\langle BB^*\rangle - \langle B\rangle \langle B\rangle^*\right|^2}{16\pi^2 |C|^4}. \tag{3.14}$$

Note for later use that for $z > 0$

$$\begin{aligned} \psi_1^* \psi_0 = |C|^2 \Big(& e^{-i(\mathbf{k}_{1,i} - \mathbf{k}_{0,i})\cdot \mathbf{r}} \\ & + r_1 e^{-i(\mathbf{k}_{1,r} - \mathbf{k}_{0,i})\cdot \mathbf{r}} \\ & + r_0 e^{-i(\mathbf{k}_{1,i} - \mathbf{k}_{0,r})\cdot \mathbf{r}} \\ & + r_1 r_0 e^{-i(\mathbf{k}_{1,r} - \mathbf{k}_{0,r})\cdot \mathbf{r}} \Big), \end{aligned} \tag{3.15}$$

and for $z < 0$

$$\psi_1^* \psi_0 = |C|^2 t_1 t_0 e^{-i(\mathbf{k}_{1,t} - \mathbf{k}_{0,t})\cdot \mathbf{r}}. \tag{3.16}$$

Returning to the original notation, an evaluation of B in eq. (3.14) yields

$$\langle \psi_1 | V_1 | \psi_0 \rangle = \iiint \psi_1^* V_1 \psi_0 \, \mathrm{d}z \, \mathrm{d}x \, \mathrm{d}y$$

$$= \iint_S \left(\int_0^{z(x,y)>0} \psi_1^* V_1 \psi_0 \, \mathrm{d}z + \int_{z(x,y)<0}^{0} \psi_1^* V_1 \psi_0 \, \mathrm{d}z + \underbrace{\int_{z<z(x,y)}^{z>z(x,y)} \psi_1^* V_1 \psi_0 \, \mathrm{d}z}_{=0} \right) \mathrm{d}x \, \mathrm{d}y$$

$$= k_0^2 \left(1 - n^2\right) \iint_S \left(\int_0^{z(x,y)>0} \psi_1^* \psi_0 \, \mathrm{d}z - \int_{z(x,y)<0}^{0} \psi_1^* \psi_0 \, \mathrm{d}z \right) \mathrm{d}x \, \mathrm{d}y. \tag{3.17}$$

Equation (3.17) quickly turns into a complicated expression upon substitution of eqs. (3.15) and (3.16) and taking the configurational average. However, the calculation can be significantly simplified by assuming that ψ_0 and ψ_1 can be approximated by their expressions for $z < 0$ when[2] $0 < z < z(x, y)$, in effect meaning

[2] I.e. in the volume below the rough surface described by $z(x, y)$, but above $z = 0$.

that eq. (3.16) is used in *both* terms of eq. (3.17). The approximation, which was suggested by Sinha et al., is viable[3] for $Q_z\sigma \ll 1$, which is the only regime where it is necessary to go beyond the Born approximation to calculate the diffuse scattering. Consequently, eq. (3.17) becomes

$$\langle\psi_1|\, V_1 \,|\psi_0\rangle \simeq C^2 k_0^2 \left(1-n^2\right) t_1 t_0 F\left(\mathbf{Q}_t\right), \tag{3.18}$$

where $\mathbf{Q}_t = \mathbf{k}_{1,t} - \mathbf{k}_{0,t}$, and[4]

$$\begin{aligned} F(\mathbf{Q}_t) &= \iint_S \int_0^{z(x,y)>0} e^{-i\mathbf{Q}_t\cdot\mathbf{r}}\, \mathrm{d}z\, \mathrm{d}x\, \mathrm{d}y \\ &+ \iint_S \int_{z(x,y)<0}^{0} e^{-i\mathbf{Q}_t\cdot\mathbf{r}}\, \mathrm{d}z\, \mathrm{d}x\, \mathrm{d}y \\ &= \frac{i}{Q_{t,z}} \iint_S \left(e^{-iQ_{t,z}z(x,y)} - 1\right) e^{-i(Q_x x + Q_y y)}\, \mathrm{d}x\, \mathrm{d}y. \end{aligned} \tag{3.19}$$

Substitution of eq. (3.18) into eq. (3.14) yields for the diffuse differential scattering cross section

$$\left(\frac{\mathrm{d}\sigma}{\mathrm{d}\Omega}\right)_{\text{diff}} = \frac{\left|k_0^2(1-n^2)\right|^2}{16\pi^2}|t_1|^2|t_0|^2\left[\langle F(\mathbf{Q}_t)F^*(\mathbf{Q}_t)\rangle - \langle F(\mathbf{Q}_t)\rangle\langle F^*(\mathbf{Q}_t)\rangle\right]. \tag{3.20}$$

Under the key assumption that $z(x,y)$ describes a Gaussian random surface, $\omega\left(z\right)$ is given by eq. (3.2). The configurational averages $\langle F(\mathbf{Q}_t)\rangle$ and $\langle F^*(\mathbf{Q}_t)\rangle$ in eq. (3.20) then yield

$$\begin{aligned} \langle F(\mathbf{Q}_t)\rangle &= \frac{i}{Q_{t,z}} \iint_S \int_{-\infty}^{\infty} \omega(z)\left(e^{-iQ_{t,z}z} - 1\right) e^{-i(Q_x x + Q_y y)}\, \mathrm{d}x\, \mathrm{d}y\, \mathrm{d}z \\ &= \frac{i}{Q_{t,z}} \iint_S \left(e^{-Q_{t,z}^2\sigma^2/2} - 1\right) e^{-i(Q_x x + Q_y y)}\, \mathrm{d}x\, \mathrm{d}y \qquad (3.21) \\ \langle F^*(\mathbf{Q}_t)\rangle &= -\frac{i}{Q_{t,z}^*} \iint_S \left(e^{-(Q_{t,z}^*)^2\sigma^2/2} - 1\right) e^{i(Q_x x + Q_y y)}\, \mathrm{d}x\, \mathrm{d}y, \qquad (3.22) \end{aligned}$$

(3.23)

such that the product $\langle F(\mathbf{Q}_t)\rangle\langle F^*(\mathbf{Q}_t)\rangle$ becomes

$$\begin{aligned} \langle F(\mathbf{Q}_t)\rangle\langle F^*(\mathbf{Q}_t)\rangle = \frac{1}{|Q_{t,z}|^2} \iint_S \iint_S &\left(e^{-\left((Q_{t,z})^2 + (Q_{t,z}^*)^2\right)\sigma^2/2} - e^{-Q_{t,z}^2\sigma^2/2} - e^{-(Q_{t,z}^*)^2\sigma^2/2} + 1\right) \\ &\times e^{-i\left(Q_x(x-x') + Q_y(y-y')\right)}\, \mathrm{d}x\, \mathrm{d}y\, \mathrm{d}x'\, \mathrm{d}y'. \end{aligned} \tag{3.24}$$

[3]Evaluation of the constraint $Q_z\sigma \ll 1$ shows that it can be re-expressed as $\Omega << \arcsin\left[\lambda/(4\pi\sigma)\right]$, where Ω is the angle between the sample surface and the incident beam. This is under the assumption that at some point during a scan $Q_z \approx |\mathbf{Q}|$. For example, if $\lambda = 1.54$ Å and $\sigma = 5$ Å, then $\Omega \ll 1.4°$.

[4]Note that Q_x and Q_y are independent of the medium and remain unchanged as the wave vectors they depend on maintain their x and y components in surface scattering, cf. eq. (2.5).

The configurational average $\langle F(\mathbf{Q}_t)F^*(\mathbf{Q}_t)\rangle$ yields

$$\begin{aligned}\langle F(\mathbf{Q}_t)F^*(\mathbf{Q}_t)\rangle &= \frac{1}{|Q_{t,z}|^2}\iint_S\iint_S \left\langle \left(e^{iQ_{t,z}z(x,y)}-1\right)\left(e^{-iQ^*_{t,z}z(x',y')}-1\right)\right\rangle \\ &\quad\times e^{-i\left(Q_x(x-x')+Q_y(y-y')\right)}\,\mathrm{d}x\,\mathrm{d}y\,\mathrm{d}x'\,\mathrm{d}y' \\ &= \frac{1}{|Q_{t,z}|^2}\iint_S\iint_S \left(\left\langle e^{i\left[Q_{t,z}z(x,y)-Q^*_{t,z}z(x',y')\right]}\right\rangle - e^{-Q^2_{t,z}\sigma^2/2} - e^{-(Q^*_{t,z})^2\sigma^2/2}+1\right) \\ &\quad\times e^{-i\left(Q_x(x-x')+Q_y(y-y')\right)}\,\mathrm{d}x\,\mathrm{d}y\,\mathrm{d}x'\,\mathrm{d}y'. \end{aligned} \tag{3.25}$$

In order to solve this configurational average $[Q_{t,z}z(x,y)-Q^*_{t,z}z(x',y')]$ is taken to be a Gaussian random variable of the form $[s(x,y)-s'z(x',y')]$ so that eq. (3.3) can be used. Substituting for the relative coordinates $X=x'-x$ and $Y=y'-y$, eqs. (3.24) and (3.25) then yield

$$\begin{aligned}\langle F(\mathbf{Q}_t)\rangle\,\langle F^*(\mathbf{Q}_t)\rangle &= \frac{S}{|Q_{t,z}|^2}\iint_S\left(e^{-\left((Q_{t,z})^2+(Q^*_{t,z})^2\right)\sigma^2/2}\right. \\ &\quad\left.-\,e^{-Q^2_{t,z}\sigma^2/2}-e^{-(Q^*_{t,z})^2\sigma^2/2}+1\right)e^{i(Q_xX+Q_yY)}\,\mathrm{d}X\,\mathrm{d}Y \end{aligned} \tag{3.26}$$

$$\begin{aligned}\langle F(\mathbf{Q}_t)F^*(\mathbf{Q}_t)\rangle &= \frac{S}{|Q_{t,z}|^2}\iint_S\left(e^{-\left((Q_{t,z})^2+(Q^*_{t,z})^2\right)\sigma^2/2+|Q_{t,z}|^2C(X,Y)}\right. \\ &\quad\left.-\,e^{-Q^2_{t,z}\sigma^2/2}-e^{-(Q^*_{t,z})^2\sigma^2/2}+1\right)e^{i(Q_xX+Q_yY)}\,\mathrm{d}X\,\mathrm{d}Y. \end{aligned} \tag{3.27}$$

Substituting eqs. (3.26) and (3.27) into eq. (3.20) finally yields for the diffuse differential scattering cross section

$$\boxed{\left(\frac{\mathrm{d}\sigma}{\mathrm{d}\Omega}\right)_{\text{diff}} = \frac{S\left|k_0^2(1-n^2)\right|^2}{16\pi^2}|t_1|^2|t_0|^2P(Q_x,Q_y)} \tag{3.28}$$

where

$$P(Q_x,Q_y) = \frac{e^{-\left((Q_{t,z})^2+(Q^*_{t,z})^2\right)\sigma^2/2}}{|Q_{t,z}|^2}\iint_S\left(e^{|Q_{t,z}|^2C(X,Y)}-1\right)e^{i(Q_xX+Q_yY)}\,\mathrm{d}X\,\mathrm{d}Y, \tag{3.29}$$

which for very small $Q_{t,z}$ (i.e. $Q_z\sigma \ll 1$) can be approximated to yield

$$P(Q_x,Q_y) \simeq \iint_S C(X,Y)e^{i(Q_xX+Q_yY)}\,\mathrm{d}X\,\mathrm{d}Y. \tag{3.30}$$

Table table 3.1 lists the various approximations and assumptions taken in the preceding derivation of eq. (3.28).

Table 3.1: An overview of the physical and mathematical compromises implicit in eq. (3.28) that lead to uncertainties.

TE-polarization	In the derivation of the Fresnel equations in section 2.2, transverse electric polarized radiation was assumed. This is a good assumption for two reasons. Firstly, the Fresnel equations are to a large degree independent of polarization at small angles. Secondly, X-ray synchrotrons predominantly emit horizontally polarized radiation.
χ_α replaced by $\chi_{0\alpha}$	The scattered wave function χ_α is a stationary solution of the Schrödinger equation with the potential $V_0 + V_1$. However, in the derivation of the DWBA in appendix A, it was replaced by $\chi_{0\alpha}$ which is also a solution of the Schrödinger equation, but with the potential V_0.
ψ_0 and ψ_1	In the derivation of the DWBA scattering cross section for diffuse X-rays, the calculations were simplified by assuming that ψ_0 and ψ_1 could be approximated by their expressions for $z < 0$ for $0 < z < z(x, y)$. The approximation is viable for $Q_z\sigma \ll 1$.
V_0 and V_1	The choice of potential functions in section 3.3 is taken under the assumption that the electron density is constant in the x- and y-directions within a medium. A detailed discussion about scattering potentials in X-ray reflectivity is given in [13].
Gaussian random surface	In the derivation of the DWBA for X-rays incident on a rough surface, a Gaussian distribution of the relative surface heights was assumed.
$P(Q_x, Q_y)$	Equation (3.29) was approximated to yield eq. (3.30) assuming very small $Q_{t,z}$, which in practice is true so long as $Q_z\sigma \ll 1$.

3.4 Multiple Interfaces

The DWBA expression for X-ray scattering can also be derived for multilayer structures with several interfaces. Using the full set of wave equations, which is to say four eigenstates for each of the N layers, the integral over z is split up and it is found [7] that

$$\begin{aligned}\left(\frac{\mathrm{d}\sigma}{\mathrm{d}\Omega}\right)_{\text{diff}} \simeq\ & \frac{k_0^4 S}{16\pi^2} \sum_{j=0}^{N} \left|n_j^2 - n_{j+1}^2\right|^2 \\ & \times \left| \left(t_0^{j+1} t_1^{j+1} + r_0^{j+1} r_1^{j+1}\right) e^{-(\sigma j Q_{0,z}^{j+1})^2/2} \right. \\ & \left. + \left(t_0^{j+1} r_1^{j+1} + t_1^{j+1} r_0^{j+1}\right) e^{-(\sigma j Q_{1,z}^{j+1})^2/2} \right|^2 P_j(Q_x, Q_y), \end{aligned} \tag{3.31}$$

where the stacking reflection coefficients from section 2.3 provide the correct amplitudes. Here, the potentials corresponding to flat interfaces are given by

$$V_0^j = \begin{cases} k_0^2 \left(n_j^2 - n_{j+1}^2\right) & \text{for } -\infty < z < 0 \\ 0 & \text{for } z > 0 \end{cases} \tag{3.32}$$

The perturbation potential accounts for the interface roughnesses and is given by

$$V_1^j = \begin{cases} k_0^2 \left(n_j^2 - n_{j+1}^2\right) & \text{for } z_j < z < z_j + z_j(x,y) \text{ if } z_j(x,y) > 0 \\ -k_0^2 \left(n_j^2 - n_{j+1}^2\right) & \text{for } z_j > z > z_j + z_j(x,y) \text{ if } z_j(x,y) < 0 \\ 0 & \text{elsewhere} \end{cases} \tag{3.33}$$

and finally

$$P_j(Q_x, Q_y) \simeq \int_S C_j(x,y) e^{-i(xQ_x + yQ_y)}\, \mathrm{d}x\, \mathrm{d}y. \tag{3.34}$$

Equation (3.31) is based on the same assumptions and approximations as the substrate model of the previous section. Furthermore, it assumes that the surface topography functions $z_j(x,y)$ for adjacent layers are not correlated. This assumption could be fulfilled for thicker layers, while for thinner layers a certain degree of correlation could influence the scattering.

Terms in eq. (3.31) with $j > 1$ seldom contribute much to the the signal unless the layers are very thin [7]. Terms with $j > 1$ can therefore potentially be neglected for simulations of some structures. Figures 3.5 and 3.6 show the contributions from each term for two very different structures.

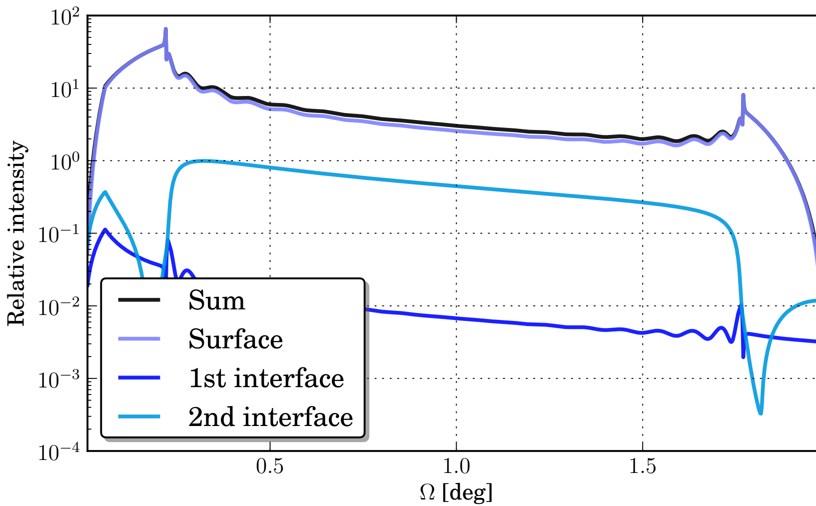

Figure 3.5: The multilayer DWBA expression, eq. (3.31), is a sum of N separate terms. For this simulated scan of an [Al_2O_3 200 Å/TiO_2 200 Å/Si] structure ($N = 3$) the term corresponding to the first interface ([Surface/ 1st interface /2nd interface]) may safely be neglected as it is about two orders of magnitude lower than the contribution from the surface. However, it is essential to have an idea of numerical precision requirements before doing such approximations. Other parameters: $2\theta = 1.99$ degree, $\sigma_j = 2$ Å, $\zeta_j = 500$ Å, h_j = 1.0, $\lambda = 1.1808$ Å.

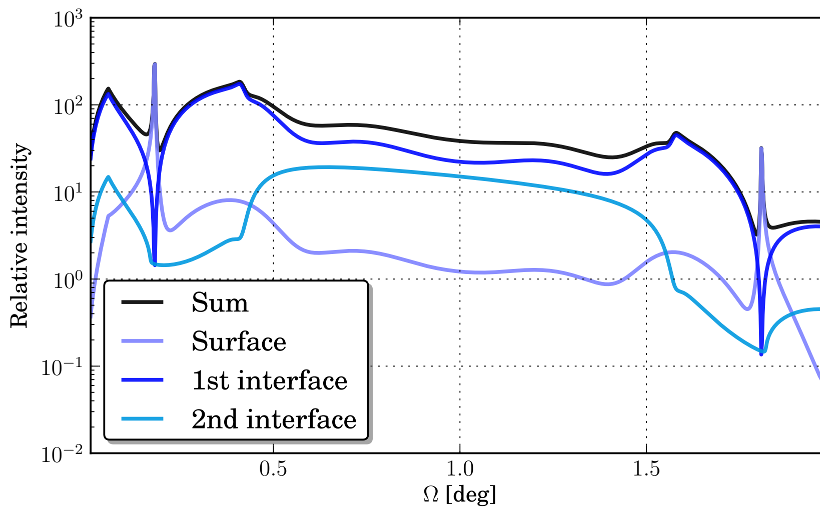

Figure 3.6: The multilayer DWBA expression, eq. (3.31), is a sum of N separate terms. For this simulated scan of a [SiO_2 5 Å/Au 100 Å/Si] structure ($N = 3$) all terms at some point lie withing the same order of magnitude ([Surface/ 1st interface /2nd interface]). Therefore, none of the terms should be neglected. Other parameters: $2\theta = 1.99$ degree, $\sigma_j = 2$ Å, $\zeta_j = 500$ Å, $h_j = 1.0$, $\lambda = 1.1808$ Å.

Chapter 4

Experimental

This chapter provides information about the samples, relevant scan methods, and the experimental setup.

4.1 Samples

Two samples have been studied, both kindly provided by Assoc. Prof. Ola Nilsen at the University of Oslo. Specifically, the samples were a [TiO_2/Si] thin film structure[1] and an [Al_2O_3/TiO_2/Si] structure, cf. table 4.1.

Table 4.1: Data for sample A and sample B. The nominal thicknesses correspond to values provided by Assoc. Prof. Ola Nilsen.

	Sample A		
	Si	TiO_2	
Nominal thickness [Å]	(Substrate)	400	
	Sample B		
	Si	TiO_2	Al_2O_3
Nominal thickness [Å]	(Substrate)	200	200

Atomic layer deposition (ALD), a thin film deposition technique based on alternate saturative surface reactions [14], was used to deposit the various layers. ALD is a type of deposition where the specimen is repeatedly exposed to alternating chemical precursors. For example, deposition of a TiO_2 layer requires two precursors, $TiCl_4$ and H_2O. The reaction chamber is purged with an inert gas such as N_2 between each step to avoid mixing of the precursors. The film grows one monolayer for each cycle.

[1] [TiO_2/Si] denotes a thin film structure consisting of a layer of TiO_2 on top of a Si substrate.

Although ALD is a slow process, each exposure and subsequent reaction is self-limited, resulting in excellent thickness control. However, the end surface might have excess precursors, and the bulk is subject to precursor contaminants.

4.2 Scan Methods

There are three common ways of grazing incidence reflectivity measurements with regard to sample and detector geometry. Figure 4.1 illustrates the geometry of a typical setup with an X-ray source, a sample, and a detector. 2θ denotes the angle between incoming beam and the detector, and Ω the angle between the incoming beam and the sample surface. ϕ_{tr} denotes the transverse angle of the detector.

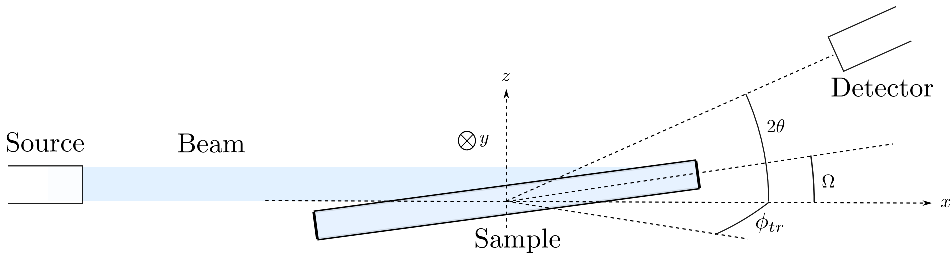

Figure 4.1: The geometry of an experimental setup for X-ray reflectivity. 2θ denotes the angle between incoming beam and the detector, and Ω the angle between the incoming beam and the sample surface. ϕ_{tr} denotes the transverse angle of the detector ($\phi_{tr} = 0$ for the depicted detector). Note that in some setups it is also possible to rotate the detector in the transverse direction (i.e. in and out of the paper plane). Doing so results in an additional nonzero component Q_y to $\mathbf{Q}$.

A *specular scan* is characterized by $\Omega = \theta$, meaning that the detector always is in the direction of the specular reflected beam. In this type of scan the specular signal dominates. Data from specular scans are commonly used in combination with multi-parameter fitting algorithms to obtain structure information.

In a *rocking scan* 2θ is fixed at some angle, and the sample rotation, Ω, is free. The specular condition is only fulfilled at $\Omega = \theta$, resulting in a sharp peak around this angle. However, at other angles only the diffuse signal and background radiation is detectable, cf. eq. (3.31). The final type of scan has Ω fixed, but 2θ is free, and is referred to as a *detector scan*. While the scan methods listed so far only require a small point-like detector, it is also possible to conduct scans with one- or two-dimensional detectors.

Figure fig. 4.2 shows examples of the characteristic paths taken in *Q-space* by each type of scan. Here, $\mathbf{Q}$ is the momentum transfer between the source wave

and detector wave, cf. section 3.3. Q_x and Q_z denote the x and y components of $\mathbf{Q}$ with respect to the sample surface.

At this point it should be noted that the incident beam possesses cross section. For example, the data used in this thesis was obtained using a beam with rectangular cross section and a Gaussian intensity profile. The characteristics of the cross section introduce some additional considerations that must be addressed in the data analysis, cf. fig. 4.3. Firstly, when the beam is almost parallel to the sample surface, part of the beam does not contribute, thus reducing the intensity compared to angles where a larger extent of the beam strikes the surface. The intensity profile must also be taken into account. Secondly, the illuminated area on the sample surface, called the *footprint*, depends on the incident angle of the beam, which has consequences for the area over which the integral is taken in eq. (3.34). Finally, there is always some *background* noise to consider.

4.3 W1 Beamline Characteristics

The experimental data was obtained at Hamburger Synchrotronstrahlungslabor (HASYLAB) at Deutsches Elektronen-Synchrotron (DESY) using the W1 (ROEWI) beamline. The W1 beamline boasts a $4 - 11.5$ keV focused-beam energy range. 10.5 keV was used, resulting in a wavelength of 1.1808 Å. A 70 mm long one-dimensional linear detector consisting of an array of 1280 pixels oriented horizontally was used. The distance from the sample holder to the detector was 897 mm, meaning the detector captured data from a $4.46°$ transverse angle centered on the direct signal. X-rays striking the outer pixels of the detector have a non-negligible component Q_y in addition to Q_x and Q_y. Figures 4.4 and 4.5 illustrate the situation. Data from a scan of the direct beam, cf. fig. 4.6, indicates a 60 pixel extent (3.3 mm) of the beam in the transverse y-direction, and shows a rough intensity profile. For simplicity the beam height was taken to that of the final slit opening, i.e. 0.05 mm.

Figures 6.8 to 6.15 contain experimental data, where the data is restricted to the 60 pixels in the center of the detector to be able to simplify the simulations by assuming $Q_y \approx 0$.

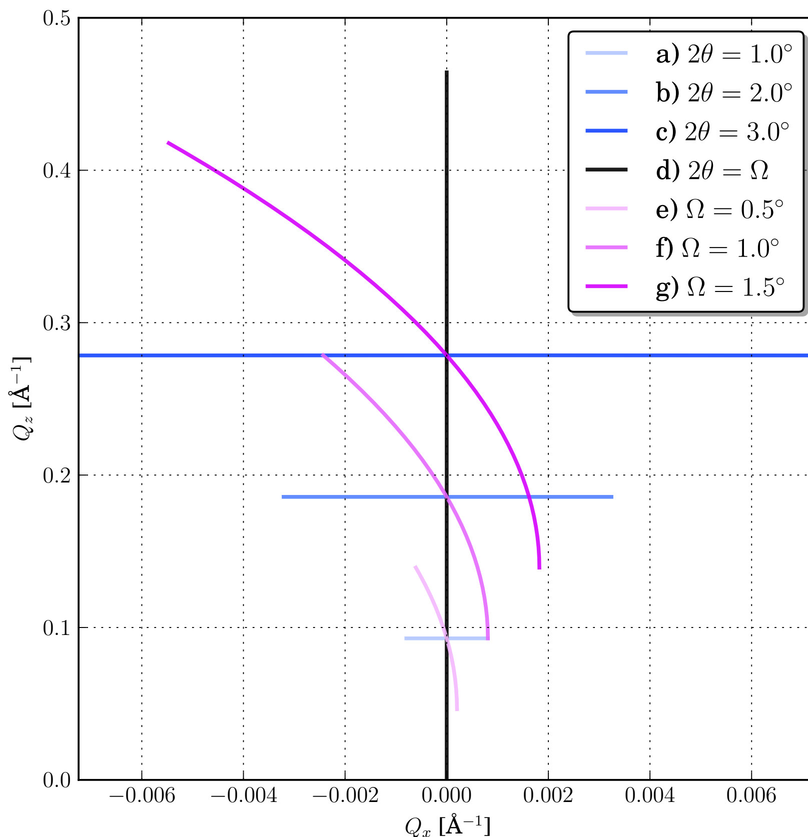

Figure 4.2: The different types of scans discussed in the text take different paths in Q-space. **(a - c):** Rocking scans at various values of 2θ. There is a small change in Q_z that is not visible here. **(d):** A specular scan for which $Q_x = 0$. **(e - g):** Detector scans for various fixed Ω where the detector is blocked below the horizon of the sample (Q_z does not reach zero). Note that the axes are of quite different scales. $\lambda = 1.1808$ Å. The DWBA used in this thesis is valid in the regime where $Q_z\sigma \ll 1$.

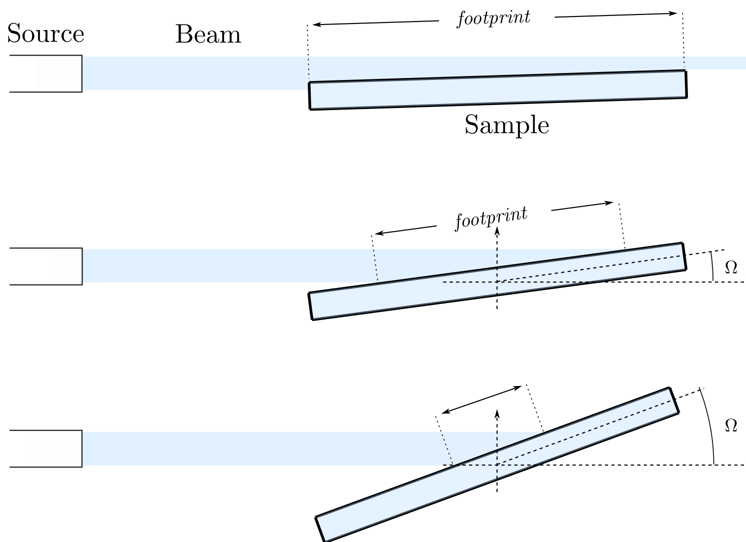

Figure 4.3: The area that gets illuminated by the beam for a certain sample rotation is called the *footprint*. As is evident from the figure, the size of the footprint changes with geometry. Note that for some angles, such as in the topmost drawing, only a small part of the incoming intensity strikes the surface and contributes to the scattered signal. This is compensated for in the computer model.

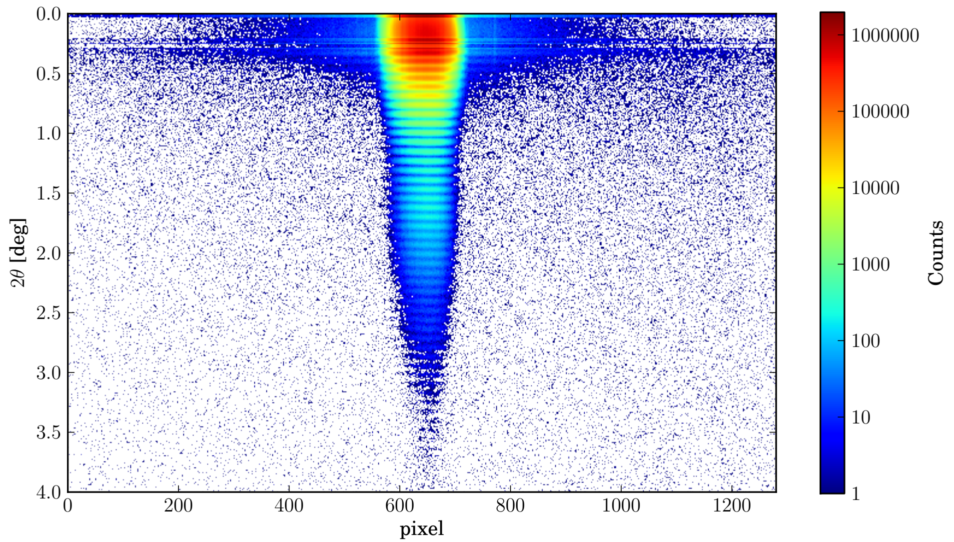

Figure 4.4: Specular scan of sample A. The detector is an array of 1280 pixels oriented along the transverse y-direction. The specular signal is in the center pixels. See also fig. 6.7a.

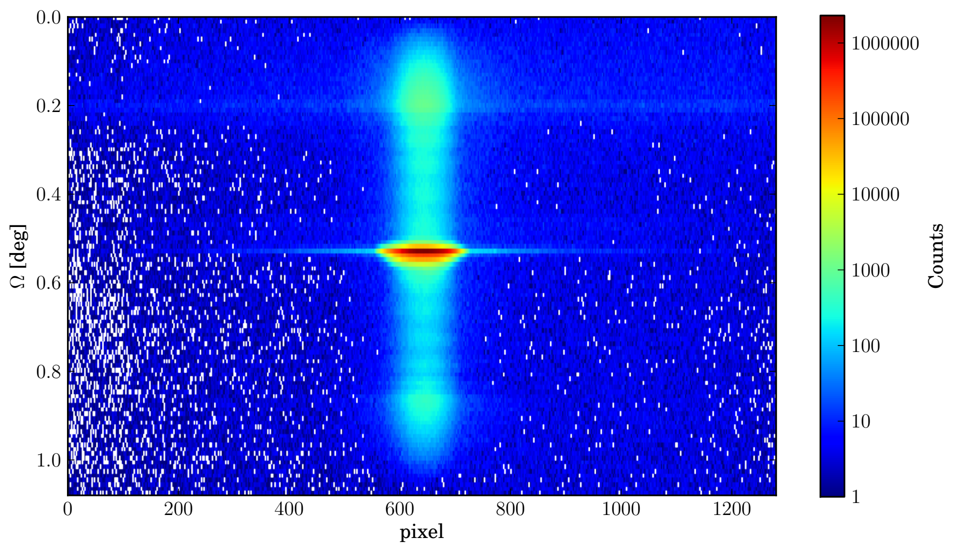

Figure 4.5: Rocking scan at $2\theta = 1.08°$ of sample A. See also fig. 6.8.

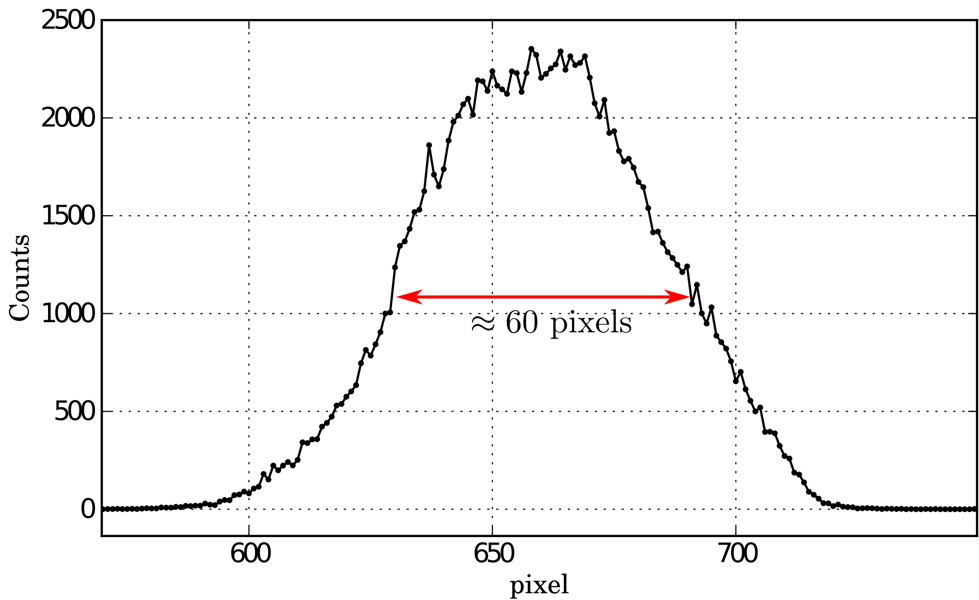

Figure 4.6: The profile of the direct beam. The horizontal axis corresponds to the pixels of the linear detector. The detector array, oriented along the transverse y-direction, was $70\,\mathrm{mm}$ broad and had 1280 pixels. This data gives an idea of the extent and intensity profile of the beam in the transverse direction. A *full width at half maximum* estimate gives a beam width corresponding to 60 pixels ($3.3\,\mathrm{mm}$).

Chapter 5

Computer Simulation

Based on the multilayer DWBA eq. (3.31), we have implemented simulation software in Python [15], a high level programming language that is both user-friendly and versatile[1]. This chapter goes through the basics of the model and proceeds to briefly explain the modular framework.

5.1 Model

The model, based on eq. (3.31), of course inherits all the uncertainties that come as a consequence of the physical and mathematical assumptions that were taken in chapter 3. There are, in addition, uncertainties related to computer precision and the numerical evaluation of Fourier transforms. Tables 3.1 and 5.1 give an overview. While many of the shortcuts listed in table 3.1 impose limitations on the model, it should be clear that removing any of them would be accompanied by an increase in the complexity of the calculations.

Beyond eq. (3.31) the model includes corrections associated with experimental X-ray (synchrotron) setups that relate to geometry, beam footprint, sample size and background radiation, cf. chapter 4.

5.1.1 Computing Fourier Transform Integrals

The Fourier transform-like integrals in eq. (3.34) are of particular interest as they cannot easily be evaluated analytically with the chosen correlation function of eq. (3.5), and therefore must be found numerically. Moreover, the integration surface, S, which is taken to be equal to the footprint, depends on the incident angle of the beam. The latter property effectively rules out[2] the option of using a fast Fourier

[1] There are Python wrappers for a number of low-level programming languages, such as C, OpenCl, OpenGL, and CUDA. The wrappers allow for the developer to code demanding tasks in fast, low-level languages while largely retaining Python's clean syntax and unifying role in the code hierarchy.

[2] The FFT relies on constant integration area.

Table 5.1: An overview of the numerical compromises inherited by the computer model that lead to uncertainties.

Machine precision	Precision can be defined as the smallest floating point number ϵ that, when added to the floating point number 1.0, produces a number different from 1.0. For double precision 64-bit floating point numbers, which are used here, $\epsilon \approx 2.22 \times 10^{-16}$ [16].
Fourier transform	The numerical evaluation of the Fourier transform of eq. (3.34) can be made more accurate by applying correction terms and oversampling, but there will always be some additional error associated with this type of computations. This is further discussed in section 5.1.1

transform algorithm (FFT), but, as it will be shown, can be disregarded when the Hurst exponent is above a certain limit (typically $h > 0.1$).

Equation (3.5) and thus eq. (3.34) are symmetric[3] in $r = \sqrt{x^2 + y^2}$ and can be re-expressed in polar coordinates :

$$P(Q_r) = 2\pi \int_0^{r_{lim}} C(r) e^{-iQ_r r} r \, \mathrm{d}r, \tag{5.1}$$

where r_{lim} is a radius at which $rC(r)$ becomes vanishingly small, $Q_r = \sqrt{Q_x^2 + Q_y^2}$, and

$$C(r) = \sigma^2 e^{-(\frac{r}{\zeta})^{2h}}. \tag{5.2}$$

However, this formalism cannot be used when r_{lim} extends beyond the boundary of the footprint, since the integration surface is strictly circular. Furthermore, if $h = 0$ then $rC(r) \propto r$ and therefore never vanishes. If r_{lim} extends beyond the footprint, then eq. (3.34) should be employed instead (integral over x and y). Figure 5.1 shows the function $rC(r)$ in the interval $0 \leq r \leq r_{lim}$ and the corresponding Fourier transform.

An intuitive way of solving a Fourier integral numerically is to split it into M subintervals:

$$F(\omega) = \int_a^b f(t) e^{-i\omega t} \, \mathrm{d}t \approx \Delta \sum_{j=0}^{M-1} f_j e^{-i\omega t_j}, \tag{5.3}$$

[3]Here we use $X = -x$ and $Y = -y$, cf. section 3.2.

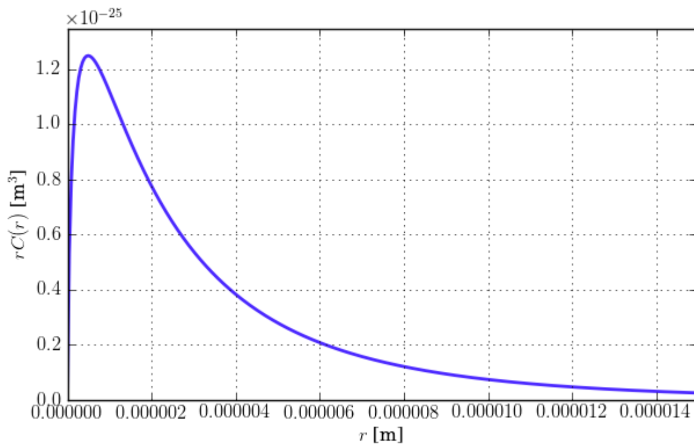

(a) The function $rC(r)$.

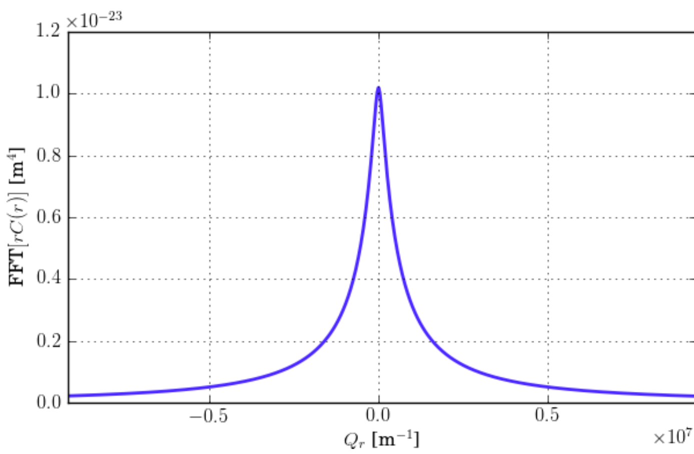

(b) The Fourier transform of $rC(r)$.

Figure 5.1: (a): The function $rC(r)$ in the interval $0 \leq r \leq r_{lim}$ with $\zeta = 500$ Å and $h = 0.2$. (b): The Fourier transform of the function in (a) resulting from FFT.

where

$$\Delta \equiv \frac{b-a}{M} \tag{5.4}$$

$$t_j \equiv a + j\Delta \tag{5.5}$$

$$f_j \equiv f(t_j). \tag{5.6}$$

For certain values of ω and M, the sum in eq. (5.3) can be made into a discrete Fourier transform (DFT) that can be evaluated using an FFT algorithm. Let M be an integer power of 2 and

$$\omega_m \Delta \equiv \frac{2\pi m}{M} \qquad m = 0, 1..., \frac{M}{2} - 1. \tag{5.7}$$

Equation (5.3) then becomes

$$F(\omega_m) \approx \Delta e^{-i\omega_m a} \underbrace{\sum_{j=0}^{M-1} f_j e^{-2\pi i m j/M}}_{\text{DFT}}. \tag{5.8}$$

This approximation is not very good for one reason. The oscillations in $e^{2\pi i m j/M}$ from $j = 0$ to $j = M - 1$ results in exactly m oscillations, meaning that larger frequencies, such as $\omega_{M/2-1}$, will oscillate $M/2 - 1$ times over an interval of M samples. In other words, the accuracy is inverse proportional to m. The situation can be remedied in two ways: By introducing correction terms of various order [16], and by "zero-padding" the array of f_j's.

Zero-padding increases the frequency resolution and is actualized by choosing an integer number $N > M$ that is a power of 2 and appending zeros to the array of f_j's for $M+1 < j \leq N-1$. The larger the N is chosen, the finer the sampling in in frequency space, whereas M determines the highest frequency sampled. Equation (5.3) becomes

$$F(\omega_n) \approx \Delta e^{-i\omega_n a} \sum_{j=0}^{N-1} f_j e^{-2\pi i n j/N}, \tag{5.9}$$

where Δ is still given by eq. (5.4), and

$$\omega_n \Delta \equiv \frac{2\pi n}{N} \qquad n = 0, 1..., \frac{N}{2} - 1. \tag{5.10}$$

Note that M no longer needs to be a power of two. Since there are N different $F(\omega_n)$'s, all of which require N iterations, the number of necessary operations to compute the DFT is proportional to N^2. The FFT algorithm reduces this factor to $N \log_2(N)$, cf. appendix B.

5.1.2 Fourier Integrals in the Model

Figure 4.3 shows that the footprint depends on the incident angle of the beam. Consider fig. 5.2. It shows how large a circle can be spanned by r_{lim} before it extends across the boundary. Recall that r_{lim} is a distance at which the function $rC(r)$ comes sufficiently close to zero. Moreover, note that $rC(r)$ for any $h > 0$ has only one maximum, the location of which, denoted r_{max}, can be found by evaluating the differential

$$\left. \frac{\mathrm{d}rC(r)}{\mathrm{d}r} \right|_{r=r_{max}} = 0 \tag{5.11}$$

and substituting for r with r_{max}. Defining the parameter $p \equiv r_{lim}C(r_{lim})/r_{max}C(r_{max})$, r_{lim} is readily found numerically through

$$r_{lim}C(r_{lim}) = p r_{max}C(r_{max}). \tag{5.12}$$

Whenever r_{lim} is within the footprint, it is safe to use eq. (5.1) and calculate it

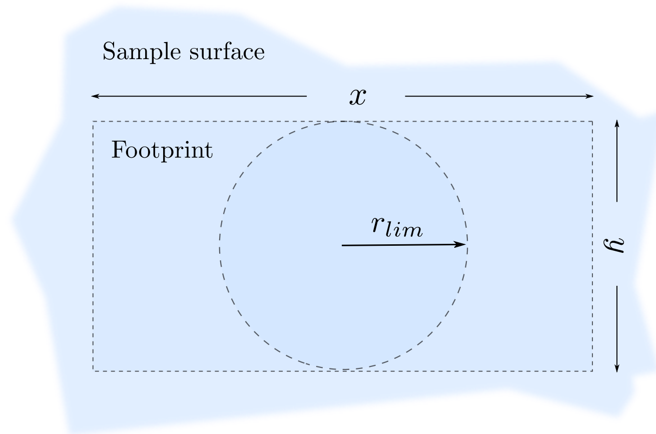

Figure 5.2: In most experimental setups the beam strikes only part of the sample surface, as seen here. The footprint is bounded by x and y. Moreover, the inner circle shows how large a value r_{lim} can take before the radial symmetry of the correlation function $C(r)$ can no longer be exploited. At this point it becomes necessary to take a two-dimensional Fourier transform over x and y, as opposed to a one-dimensional one over the r.

numerically as an FFT using the formalism of eq. (5.9) in addition to correction terms of sufficient order. However, the latter requirement of r_{lim} is not always the case. Figure 5.3 shows that r_{lim} quickly increases for small values of h.

The latter method is limited to circular footprints or cases when the actual shape of the footprint can be neglected because $rC(r)$ vanishes at its edges. When r_{lim} extends beyond the boundary we employ the standard DFT of eq. (5.9) in two

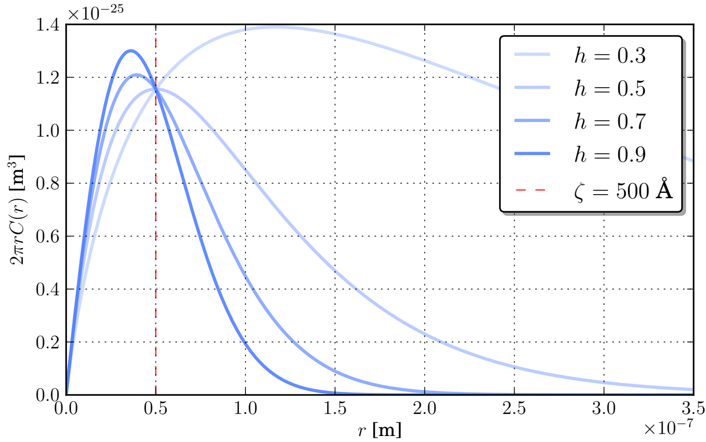

Figure 5.3: The function $2\pi rC(r)$ for different values of the Hurst exponent h. The value r_{lim} at which the function comes appreciably close to zero is clearly inverse proportional to h. The consequence is that the radial symmetry cannot be used for small values of h due to the non-circular shape of the footprint.

dimensions, x and y, taking care to change the the f_j's according to changes in the footprint. With this approach, the Fourier integral can be evaluated with any shape of the footprint. However, it remains an open question whether h actually goes low enough for actual samples that r_{lim} exceeds the footprint.

Even though r_{lim} may well exceed the correlation length ζ, or even the extent of the coherence domain of the beam, it appears to only be a mathematical effect[4]. Therefore, there should be no requirement that r_{lim} must be smaller than or bounded by the coherence length of the beam (like ζ).

In the special case when r_{lim} extends beyond the boundary, but the boundary remains stationary (i.e. only moving the detector), the two-dimensional DFT can be calculated as an FFT since the f_j's do not change.

5.2 Implementation

The Python based framework used to compute eq. (3.31) is highly modular, meaning each major function resides in a separate file for easier handling. Due to its modularity, the code can easily be extended upon or be put into other frameworks. For instance, a natural extension would be a multi-parameter fitting software to search for physical parameters that would give a good fit between the DWBA and some experimental data. Figure 5.4 gives an overview of the module hierarchy. The code is largely based on the *numpy* package [17] (numerical Python)

[4]The function $2\pi rC(r)$ extends much further than $C(r)$, but only due to the purely mathematical prefactor r.

which greatly speeds up array operations compared to the native array processes in Python.

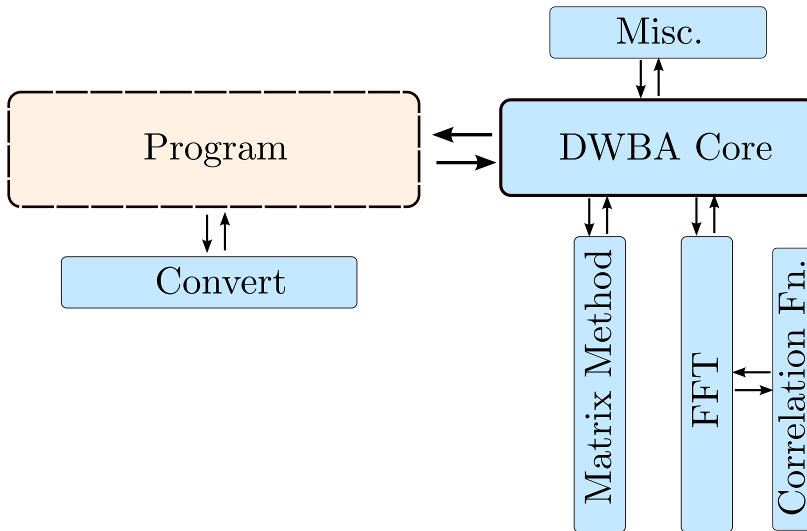

Figure 5.4: The module hierarchy of the simulation software. The optional *convert* module handles translation from the spherical coordinates Ω and 2θ to components in Q-space used by the other modules. *DWBA core* takes as input from a program sample data, beam characteristics, and an array of $\mathbf{Q}$ vectors for which the DWBA expression will be calculated, cf. eq. (3.31). It depends on the *Matrix Method* and *FFT* modules to handle wave amplitudes and Fourier inegrals.

Chapter 6

Results and Discussion

6.1 Model - General Observations

This section looks at the general features of a computer simulated small angle rocking scan of a thin film. It then proceeds to discuss the effects of changing various parameters in the model, such as surface roughness and the refractive indices.

6.1.1 Small Angle Rocking Scan

This section shows how key parameters affect the results produced by the implemented DWBA model. Figure 6.1 shows a simulated rocking scan around $2\theta = 2.0$ ° for an [Au (200 Å)/Ti (800 Å)/Si][1] thin film structure. There are several features to be noted for this example simulation that are characteristic not only for the particular structure. During a rocking scan, which is described in chapter 4, the detector is fixed at a position 2θ. Then, for small angle studies of thin films, the sample is rotated by a few degrees. At low Ω, the surface is parallel to the beam such that only background radiation is registered by the detector, (Although in figs. 3.5 and 6.1 to 6.6 the contribution from background radiation has been disregarded as it does not give useful information about the sample).

As the sample rotates and Ω increases, more of the surface intersects the beam and gives rise to an increasingly stronger signal until, in most cases, the sample catches all of the incoming intensity. In addition, the diffuse signal grows stronger as Ω approaches the specular point at $\theta = 1°$. However, it begins to decrease when the angle between the surface and the incident wave goes beyond a certain threshold, namely the critical angle, denoted Ω_c. For the structure in fig. 6.1, when $\Omega < \Omega_c = 0.415$ °, there is total internal reflection, cf. section 2.1.1, meaning that most of the incoming energy is reflected back without entering the surface.

[1][Au (200 Å)/Ti (800 Å)/Si] denotes a thin film structure consisting of 200 Å of Au on 800 Å of Ti on top of a Si substrate.

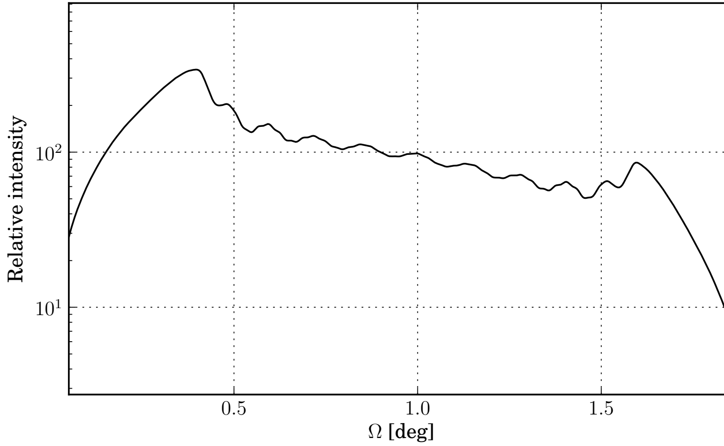

Figure 6.1: A simulated small angle rocking scan showing only the diffuse scattering from a [Au (200 Å)/Ti (800 Å)/Si] structure. Other parameters: $2\theta = 2.0\,°$, $\sigma_j = 4$ Å, $\zeta_j = 400$ Å, $h_j = 0.5$, $\lambda = 1.1808$ Å.

Beyond Ω_c the beam enters the multilayer structure, weakening the reflected signal due to transmission (most of the transmitted flux is eventually absorbed). The two peaks located at the critical angle on either side in fig. 6.1 are referred to as *Yoneda peaks* [18]. They originate from the combined effects of reflection and refraction as discussed above. Note that the second Yoneda peak appears not because of total internal reflection of the incoming beam, but rather because of the total internal reflection of the diffusively scattered waves below the critical angle, as this radiation has not been mitigated by losses into the sub-surface structure.

The oscillating features *between* the two Yoneda peaks are thickness fringes that become apparent in the interval of Ω where there is transmission into the sample. They result from interference effects between diffuse scattering from different layers, meaning they only appear for structures with at least one layer on top of the substrate. The low frequency fringes in fig. 6.1 result from interference in the thin Au layer, while the high frequency fringes that are discerned upon careful inspection can be said to originate from the much thicker Ti layer.

Around $\Omega = \theta = 1.0\,°$ the specular condition is fulfilled, and there should be a sharp peak, as will be seen in the experimental data. However, the computer model only calculates the *diffuse* component of the reflected intensity, and therefore not the specular peak. Also, note that with increasing Ω the area of the beam footprint, S, gets smaller. As a consequence, the off-specular signal diminishes according to eq. (3.31).

6.1.2 Changing Model Parameters

Equation (3.31) has many parameters that are likely to change from one sample to the next and from one experimental setup to the other. This section highlights the consequences of changing some of them. Or, specifically, those that are usually considered as *free parameters* in the model. Other parameters, such as the beam and sample geometries, are *fixed parameters*, i.e. values that are known beforehand and are not changed (by much) during the fitting procedure. This discussion serves as background material for section 6.2 where simulations are fitted to experimental data.

For the structure associated with the simulations in figs. 6.2 to 6.6, all parameters are the same except for the one which is being monitored. Specifically the figures depict rocking scan simulations of a substrate at $2\theta = 1.99°$, with $\sigma = 10\,\text{Å}$, $\zeta = 1000\,\text{Å}$, $h = 0.5$, $\delta = 1 \times 10^{-5}$, and $\beta = 1 \times 10^{-7}$. One could pose the question whether the changes induced in *one* simple substrate model are generally valid for other and perhaps more complex structures with several layers. Given the form of eq. (3.31), in which the contributions from the layers constitute separate terms, it is safe to say that parameter changes for one term (layer) will produce the same variations as for the substrate model, but that the after summation of the remaining terms their sum will not necessarily appear to have changed in the same manner.

6.1.2.1 Surface Roughness

Figure 6.2 shows the effect of varying the surface roughness. It appears that as σ increases from zero, the strength of the diffuse signal also increases, but only up to a certain point, after which the signal begins to decay. Moreover, the Yoneda peaks become increasingly pronounced. There is no diffuse scattering from a perfectly smooth surface. If, however, the surface becomes increasingly rough, there is a natural increase of the diffuse signal from zero. The decay at larger values of σ is due to the factors $e^{-(\sigma j Q_{0,z}^{j+1})^2/2}$ and $e^{-(\sigma j Q_{1,z}^{j+1})^2/2}$ in eq. (3.31).

6.1.2.2 Refractive Index

Figure 6.2 shows the effect of varying δ in the refractive index, $n = 1 - \delta + i\beta$. Evidently, doing so has a direct effect on the critical angle, as seen from the displaced Yoneda peaks. This behavior is covered in many introductory optics books [8].

When δ decreases, so does the magnitude of the diffuse signal. This is due to the choice of the potential functions in eqs. (3.32) and (3.33) which are both proportional to $n_j^2 - n_{j+1}^2$. When the refractive index of the substrate becomes increasingly similar to that of the surrounding vacuum, the scattering potentials get weaker. However, logic dictates that the reflected signal at angles of total internal reflection should remain constant despite changes in δ. This is not the case in the simulations, and it leaves some doubt about the choice of the potential functions.

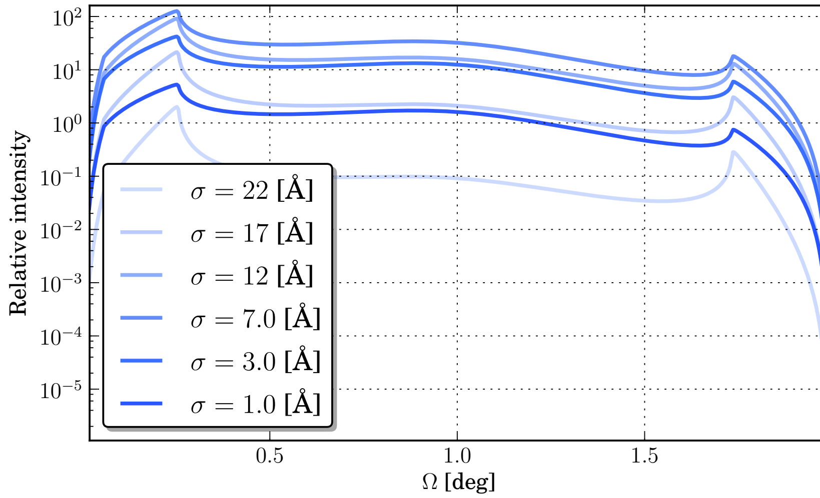

Figure 6.2: Simulated small angle rocking scans of a substrate for different root mean square roughnesses σ.

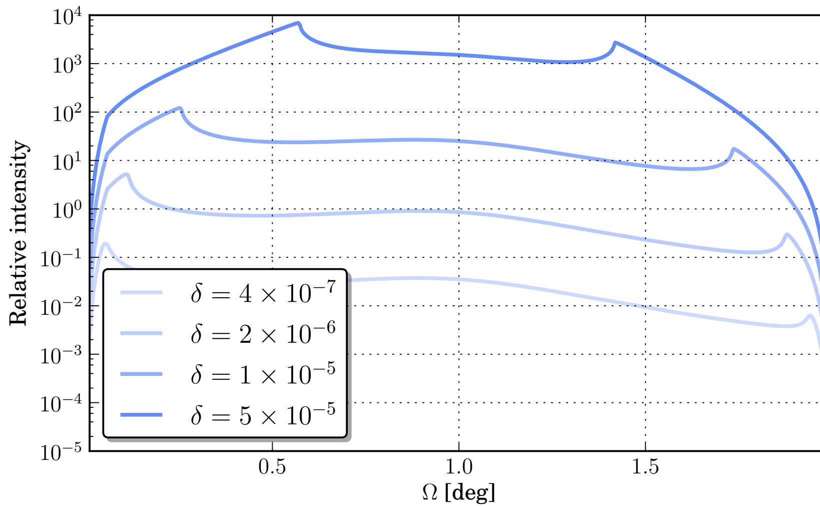

Figure 6.3: Simulated small angle rocking scans of a substrate for different δ. δ is related to the refractive index through $n = 1 - \delta + i\beta$.

Changing the imaginary part of the refractive index, β, appears to smoothen the Yoneda peaks, cf. fig. 6.4. For multilayer structures, the thickness fringes also become smoother if β increases for the layers responsible for the fringes. As dis-

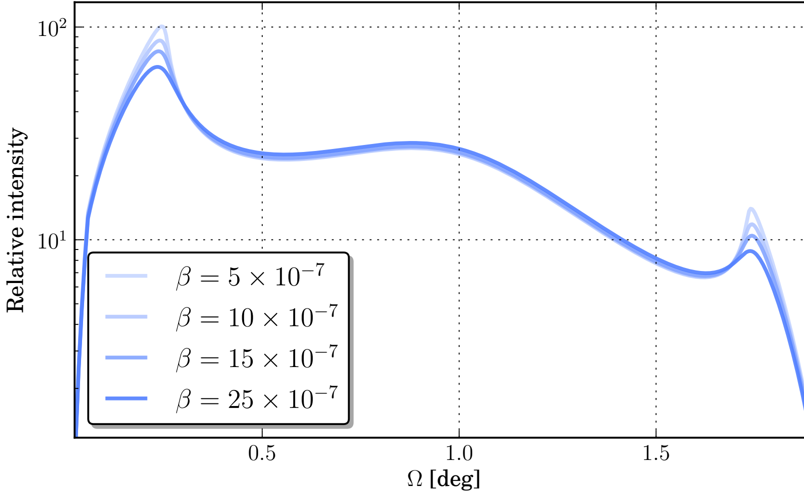

Figure 6.4: Simulated small angle rocking scans of a substrate for different β. β is related to the refractive index through $n = 1 - \delta + i\beta$

cussed in section 2.1.1, β is related to absorption losses.This results in a decreased reflected signal and a smoother transition to total internal reflection at the critical angle.

6.1.2.3 Hurst Exponent and Correlation Cut Off Length

As mentioned in section 3.3, the Hurst exponent h describes a surface of fractal dimension $D = 3 - h$. Because a flat surface has two dimensions, h takes values between zero and one. The parameter has the effect of changing the shape of the correlation function as shown in fig. 3.2, thus influencing the Fourier integral in eq. (3.34).

It appears from fig. 6.5 that a small value of h, i.e. a jagged surface with protruding features, results in a peak centered at θ , or alternatively, a peak appears because the signal decreases around θ. There is not much difference between the plots for $h > 0.5$, and it might prove difficult to determine the Hurst exponents in this range. The behavior appears not to be correlated with other parameters.

The correlation cut off length, ζ, is a key parameter in the correlation function, which describes the surface length over which features are spatially correlated in the z-direction (height direction). As can be seen in figure fig. 3.3, reducing ζ also reduces the extent of the correlation function. The Fourier integral in eq. (3.34)

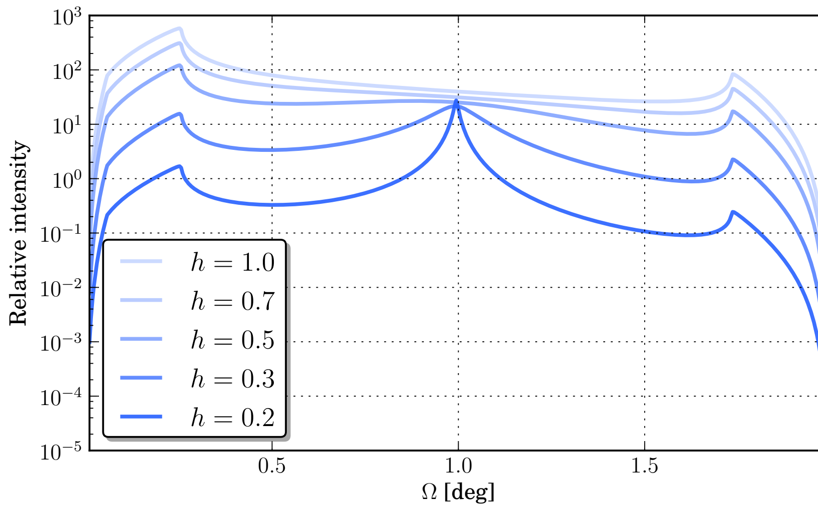

Figure 6.5: Simulated small angle rocking scans of a substrate for different Hurst exponents h. The Hurst exponent describes a surface of fractal dimension $D = 3 - h$.

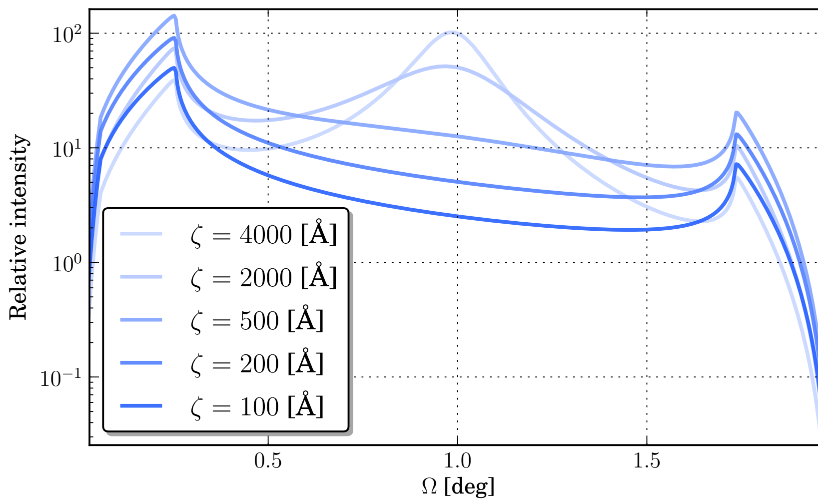

Figure 6.6: Simulated small angle rocking scans of a substrate for different correlation cut off lengths ζ.

changes accordingly. It appears that the greater the correlation length, the more the signal will be focused around $\Omega = \theta$.

6.2 Comparison With Experiment

Scattering simulations for two different thin film structures have been compared to experimental data to see whether it is feasible to determine surface specific properties of two samples within the implemented DWBA model. Data for the two samples A and B is listed in table 4.1. All refractive indices are taken from [19].

The parameters σ, ζ, and h are correlated in the implemented model [7], and it is therefore advisable to first investigate the coherent signal and determine surface roughnesses σ_j before proceeding to find the correlation lengths ζ_j and Hurst exponents h_j from the diffuse signal. The open source reflectivity program GenX [20] [2] was used to establish estimates of both the surface roughness and thickness of the two samples. Table 6.1 shows the values that were obtained. GenX is able to account for inter-diffusion between adjacent compounds in addition to surface roughness. However, inter-diffusion was eventually not taken into account for two reasons. Firstly, doing so did not improve the GenX fits, and secondly the DWBA model used here makes no distinction between inter-diffusion and roughness.

There was a tolerable degree of similarity between the model and the experimental data, cf. fig. 6.7. It has been suggested that there were irregularities in the experimental setup or in the samples influencing the reflected signal at certain angles. Moreover, data from the full length of the linear detector was used, as opposed to only the center pixels. However, the thin film thicknesses should be fairly accurate, and the surface roughnesses appear to be in the range of a few Ångström, as is to be expected given the technique used to make the samples, cf. section 4.1. The values obtained are listen in table 6.1.

Approximate fits between data and DWBA simulations were obtained using the values from table 6.1. Fits for sample A are shown in figs. 6.8 to 6.10, and for sample B in figs. 6.12 to 6.15. The parameters, listed in table 6.2, do not differ between the fits at various angles 2θ for a sample. Furthermore, r_{lim} appeared not to exceed the footprint at any point.

It can be seen from fig. 4.2 and the surface roughnesses listed in table 6.2 that the criteria $Q_z\sigma \ll 1$ is not always fulfilled and the implemented DWBA model looses its validity. However, the roughnesses are still very uncertain at this point.

The indices of refraction for the various media were changed. Decreasing δ of a medium corresponds to decreasing its electron density and shifts the Yoneda peaks outwards. Note that the model does not include the instrument resolution which to some extent should act to smoothen the simulated scans.

Although it is a cumbersome task to fit curves manually in the (present) absence of a multi-parameter fitting algorithm, some similarity between data and

[2] GenX employs a genetic algorithm to do multi-parameter fitting of reflectivity data. However, it is limited to investigations of the specular signal.

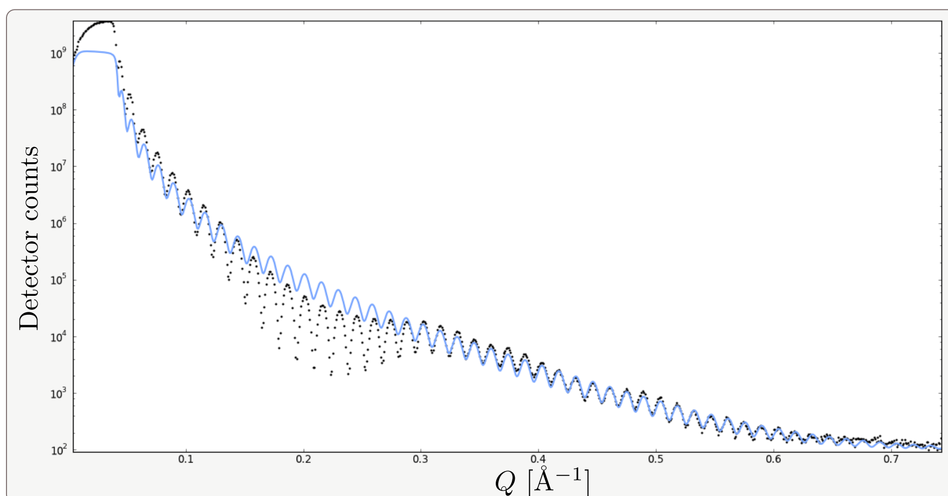

(a) Fit of a specular scan of Sample A. See also fig. 4.4.

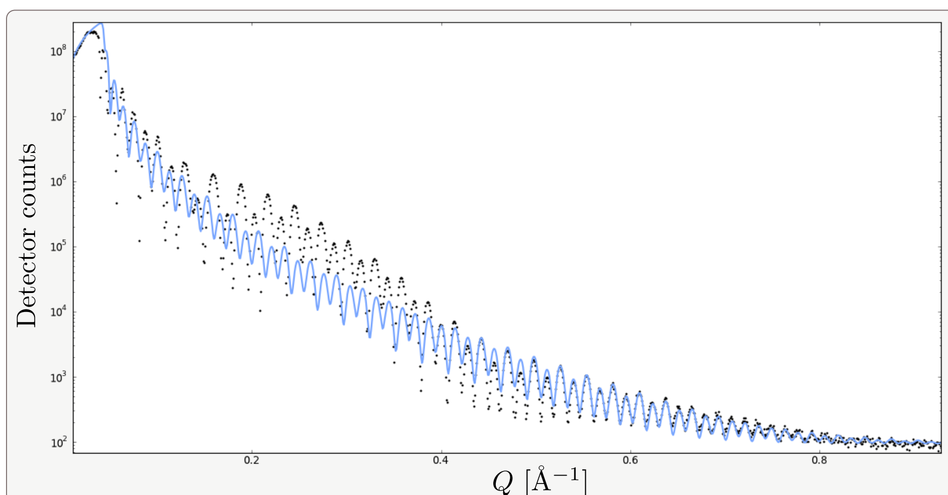

(b) Fit of a specular scan of Sample B

Figure 6.7: There was a tolerable degree of similarity between the model (blue line) and the experimental data (black dots).However, the logarithmic figure of merit functions for each plot, which is a measure of of well the model fits the data, should preferably have ended at lower values.

Table 6.1: Parameters that were obtained using the multi-parameter reflectivity fitting program GenX. Sample data is listed in table 4.1. The parameters d and σ are layer thickness and roughness, respectively. A thin layer of SiO_2 was modeled on top of the substrate in case there was some oxide formation during the making of the sample, cf. [1]. The error intervals as reported by GenX are shown in parenthesis behind each value. However, keep in mind that these are the errors as seen from the software's point of view, and that the true value of the parameters do not necessarily lie within the listed bounds. There was a tolerable degree of similarity between the model and the experimental data.The thin film thicknesses should be fairly accurate, and the roughnesses evidently lie in the Å-range.

	Sample A			
	Si	SiO_2	TiO_2	
d [Å]	∞	5.0 $(-1.8, 0.0)$	432 $(-0.8, 1.5)$	
σ [Å]	1.8 $(-1.2, 1.8)$	4.9 $(-3.0, 1.0)$	2.8 $(-0.2, 6.6)$	
	Sample B			
	Si	SiO_2	TiO_2	Al_2O_3
d [Å]	∞	3.6 $(-3.4, 1.5)$	216 $(-2.5, 2.1)$	233 $(-1.9, 2.7)$
σ [Å]	0.03 $(-0.03, 10.0)$	1.4 $(-0.41, 1.1)$	1.9 $(1.5, 2.8)$	2.3 $(-0.2, 0.1)$

model was achieved. A constant background radiation was added to the simulations. The background radiation was taken to be the magnitude of the lowest (least intense) data point in each experimental data set. Determination of the Hurst exponent form the rocking scans was complicated by the fact that the specular component covers much of the area around $\Omega = \theta$, which is the region most sensitive to changes in h, cf. section 6.1.2.3. It is therefore advantageous with a narrow and highly collimated beam to limit the extent of the specular component in the scans.

Table 6.2: An overview of the parameters used in the DWBA simulation software. Fixed parameters in bold font.

Instrument				
Wavelength		1.1808 Å		
Beam width		3.3 mm		
Beam height		0.05 mm		
Sample A				
Sample dimensions ($x \times y$)		15×30 mm^2		
	Si	SiO_2	TiO_2	
d [Å]	∞	5.00	432.00	
σ [Å]	3.60	4.90	8.40	
ζ [Å]	400.00	400.00	400.00	
h	0.40	0.40	0.40	
δ	3.76×10^{-6}	4.27×10^{-6}	6.57×10^{-6}	
β	5.15×10^{-8}	3.28×10^{-8}	2.06×10^{-7}	
Sample B				
Sample dimensions ($x \times y$)		15×30 mm^2		
	Si	SiO_2	TiO_2	Al_2O_3
d [Å]	∞	3.60	216.00	233.00
σ [Å]	0.06	2.80	3.80	6.90
ζ [Å]	1000.00	1000.00	1000.00	1000.00
h	0.40	0.40	0.40	0.40
δ	3.50×10^{-6}	3.97×10^{-6}	6.10×10^{-6}	5.84×10^{-6}
β	4.79×10^{-8}	3.05×10^{-8}	1.91×10^{-7}	3.99×10^{-8}

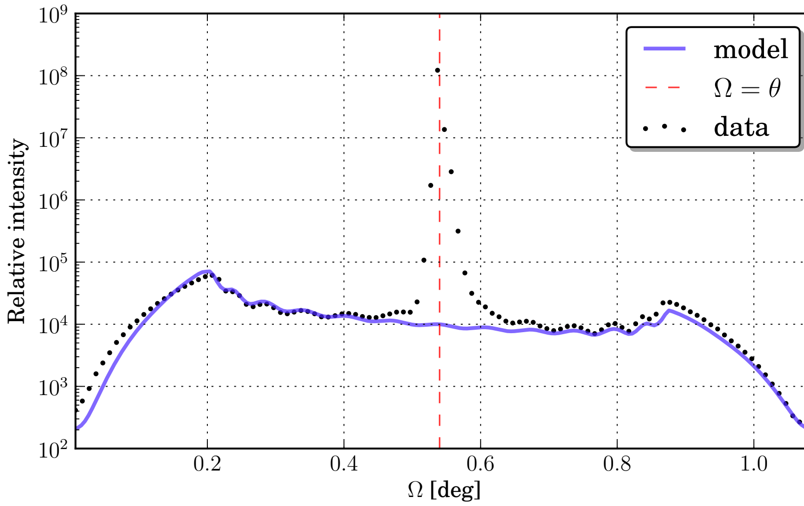

Figure 6.8: Comparison between model and data for sample A for a rocking scan around $2\theta = 1.08$ °. $Q_z\sigma \approx 0.8$. See also fig. 4.5.

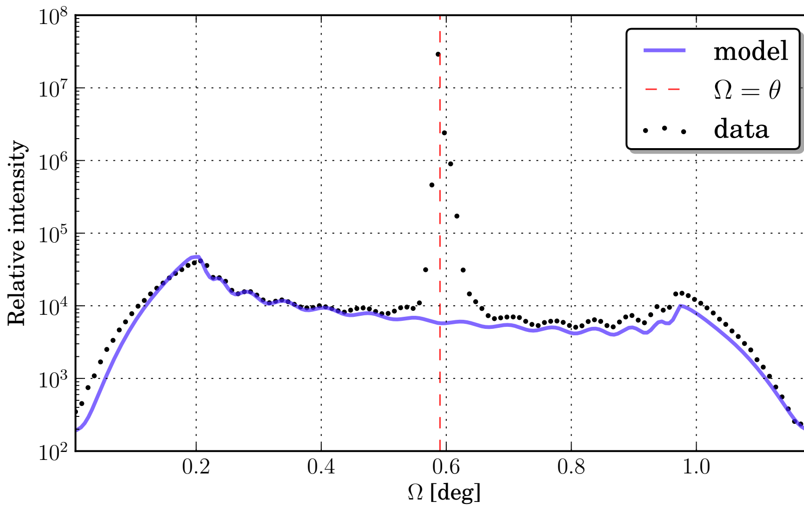

Figure 6.9: Comparison between model and data for sample A for a rocking scan around $2\theta = 1.18$ °. $Q_z\sigma \approx 0.9$.

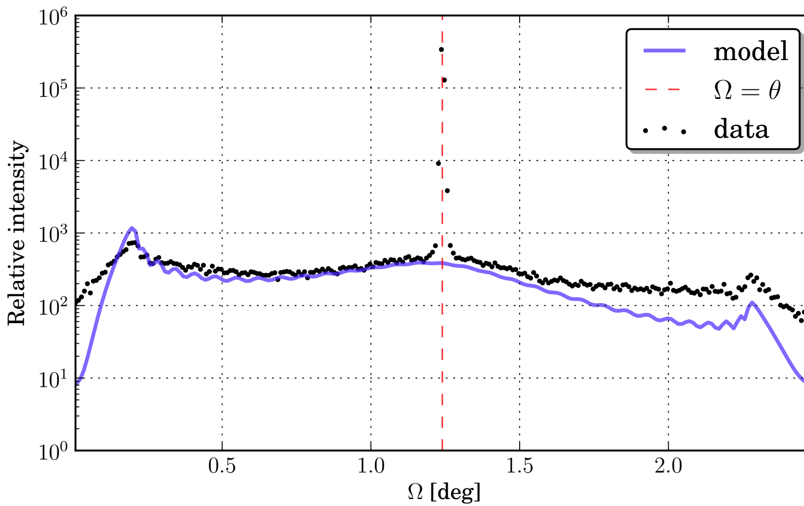

Figure 6.10: Comparison between model and data for sample A for a rocking scan around $2\theta = 2.48\,°$. $Q_z\sigma \approx 1.9$.

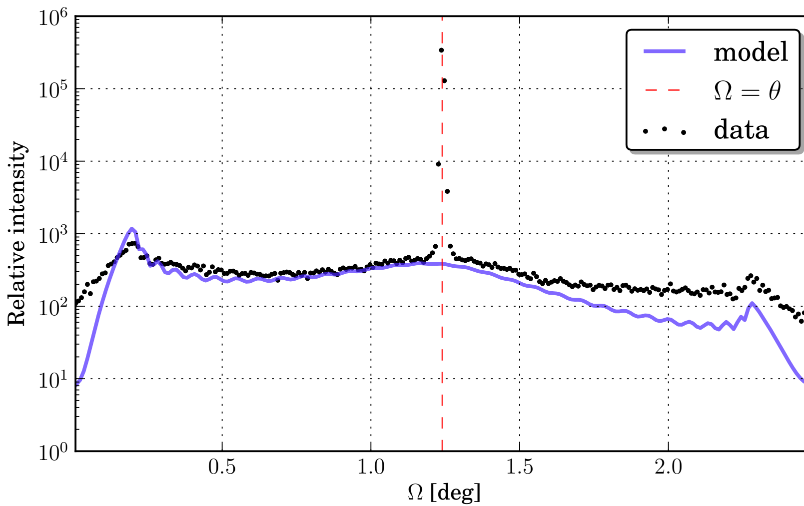

Figure 6.11: Comparison between model and data for sample A for a rocking scan around $2\theta = 2.57\,°$. $Q_z\sigma \approx 1.9$.

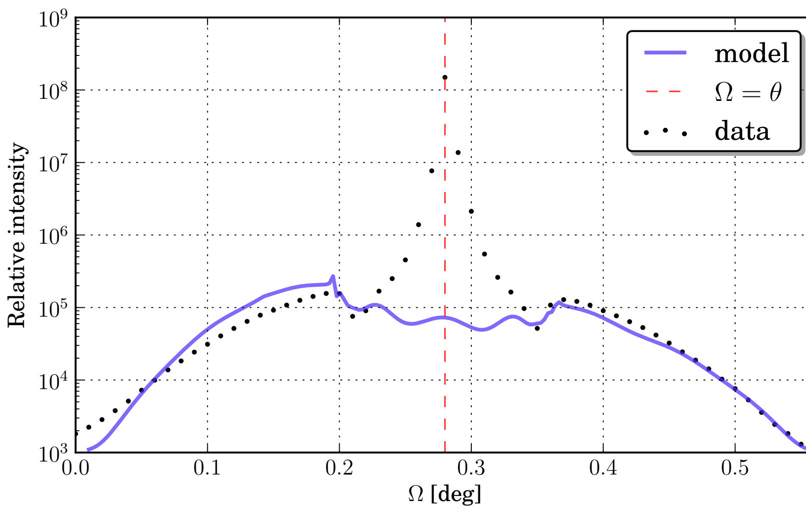

Figure 6.12: Comparison between model and data for sample B for a rocking scan around $2\theta = 0.56\,°$. $Q_z\sigma \approx 0.3$.

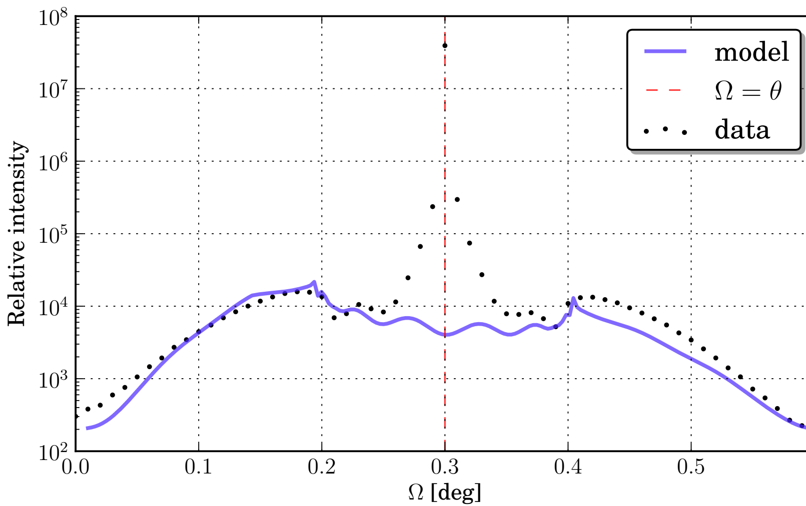

Figure 6.13: Comparison between model and data for sample B for a rocking scan around $2\theta = 0.60\,°$. $Q_z\sigma \approx 0.4$.

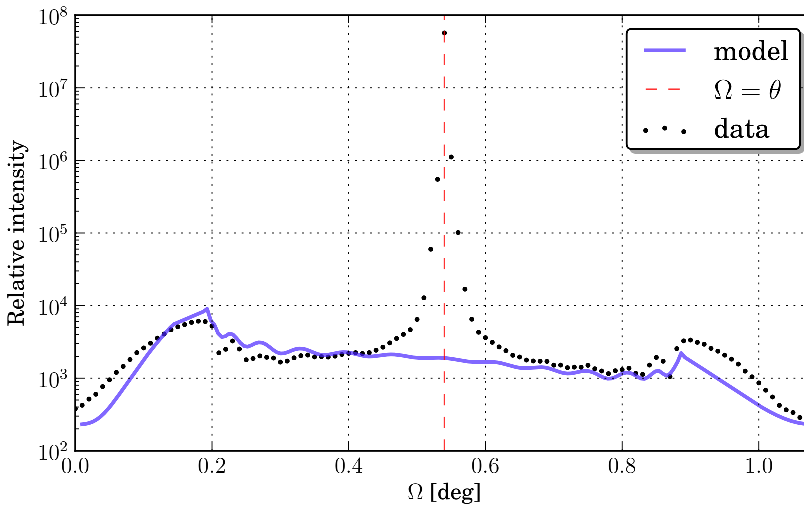

Figure 6.14: Comparison between model and data for sample B for a rocking scan around $2\theta = 1.08\,°$. $Q_z\sigma \approx 0.7$.

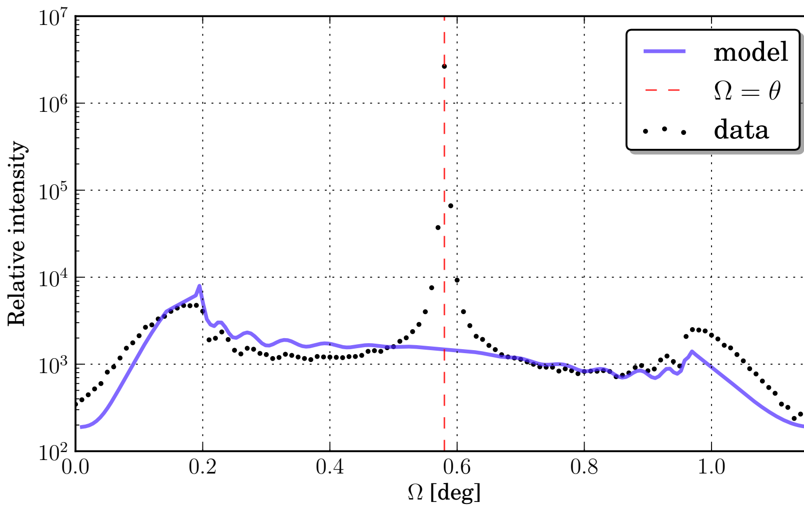

Figure 6.15: Comparison between model and data for sample B for a rocking scan around $2\theta = 1.16\,°$. $Q_z\sigma \approx 0.8$.

6.3 Outlook to Multi-parameter Fitting

To get accurate parameters more efficiently, a multi-parameter fitting algorithm should be employed.In the case of rocking scans, the figure of merit function should be weighted around the Yoneda peaks, and not at all in the interval of specular reflection in the experimental data. The algorithm should also be able to fit scans where Ω remains fixed and 2θ changes, cf. chapter 4. Moreover, it would be advantageous to combine the aforementioned with a concurrent fit of a specular scan to find the parameters that fit best not only with one, but with a number of data sets. Another possibility would be to fit two-dimensional scans at various angles, and although more computationally intensive, it would be an interesting approach as there is more data in a two-dimensional than in a one-dimensional scan.

GenX, which employs a genetic multi-parameter fitting algorithm, typically needs several thousand complete calculations of the specular reflectivity curve, or "individuals", to converge on a solution. The number is obviously highly dependent on several factors such as the number of free parameters, their respective "allowed" intervals and chance. For example, the fits in fig. 6.7 required around 7000 and 11000 individuals to converge. It is therfore important that each individual can be calculated in a reasonable amount of time.

Analyses of the implemented DWBA tools showed a typical computing time of $0.2-5$ s for a rocking scan of a structure with three layers using 500 data points. The computation time varied with the parameters h, ζ, and 2θ because they influence the time required to calculate the Fourier integrals with resolution to match the number of data points, cf. section 5.1.1. Further analysis revealed that between $90-99$ % of the time was spent solving the Fourier integrals. Optimization and parallelization [21–23] of the FFT should therefore vastly improve the computation time. Furthermore, recall that for some structures, select terms of eq. (3.31) can be disregarded as their contributions are negligible, cf. section 3.4. Performance should therefore be greatly improved when the parameters in a multi-parameter fitting algorithm became exact enough to establish which terms might safely be neglected.

Chapter 7

Conclusion

The differential scattering cross section for diffuse scattering of X-rays from thin film structures has been discussed within the framework of the distorted wave Born approximation (DWBA). In contrast to the standard Born approximation (BA), the distorted wave approach succeeds in calculating scattering from surfaces near the critical angle. The method is particularly useful for studying average surface properties.

Compromises made in the derivation of the model, cf. table 3.1, substantially simplify the final expression, but also limit its range of validity, which is determined by the requirement $Q_z\sigma \ll 1$. However, this is also the only regime where it is necessary to go beyond the simpler Born approximation. Furthermore, the rough surface (and interfaces) was taken to be a Gaussian random surface, which naturally leads to the inclusion of a desired height-height correlation function. A height-height correlation function with a correlation length cut off parameter ζ was used, as suggested by Sinha et al. [6].

A computer simulation software based on the aforementioned DWBA expression has successfully been implemented in Python. Specifically, the model finds the differential scattering cross section of diffusively scattered X-rays from a thin film structure of N layers. The implemented DWBA depends on the surface specific parameters ζ and a Hurst exponent h. The latter parameter describes the fractal dimension of the surface features. The various effects of changing key model parameters, among them ζ and h, have been demonstrated. Work by Holý et al. suggests that the surface roughness σ is correlated with the latter two parameters [7], and the DWBA was therefore supplemented with an evaluation of the specular signal in determining the surface roughness from experimental data. Fitting of the specular signal was done within the GenX software [20].

Although emphasis was not put on searching manually for the best possible parameters, comparison between experimental data and the DWBA model looks promising. Simulations of rocking scans for different values of $h > 0.5$ are hard to distinguish, and are further complicated as the specular signal in the experimental scans is centered around the area that is most sensitive to changes in the Hurst exponent.

Multi-parameter fitting algorithms are crucial in order to efficiently match a model to the data to determine probable sample parameters. The Python implementation of the DWBA, which was programmed to be surveyable and easy-to-follow rather than fast, spends up to a few seconds to calculate a 500 data point simulation of a structure with three layers. However, most of this time is spent calculating Fourier-type integrals. Under this premise a multi-parameter fitting algorithm for the DWBA (even for 2D scans) should be feasible given proper optimization and parallelization of the fast Fourier transform (FFT) part of the code.

Recommendable future work includes optimization and parallelization of the DWBA code and implementing a decent multi-parameter fitting algorithm. The latter would preferably be placed in a flexible framework allowing simultaneous fitting of both specular scans and diffuse scans (for example rocking scans). Furthermore, it would be necessary to factor in instrument resolution as parameter and pay closer attention to the influence of the coherence properties of the incoming beam.

Bibliography

[1] Parratt, L. G. Surface studies of solids by total reflection of x-rays. *Phys. Rev.* **95**, 359–369 (1954). 1, 48

[2] PORTEUS, J. O. Relation between the height distribution of a rough surface and the reflectance at normal incidence. *J. Opt. Soc. Am.* **53**, 1394–1402 (1963). URL `http://www.opticsinfobase.org/abstract.cfm?URI=josa-53-12-1394`. 1

[3] Braslau, A. *et al.* Surface roughness of water measured by x-ray reflectivity. *Phys. Rev. Lett.* **54**, 114–117 (1985). 1

[4] Elson, J. M. Theory of light scattering from a rough surface with an inhomogeneous dielectric permittivity. *Phys. Rev. B* **30**, 5460–5480 (1984). 1

[5] Glatter, O. & Kratky, O. *Small angle x-ray scattering* (Academic Press, 1982). 1

[6] Sinha, S. K., Sirota, E. B., Garoff, S. & Stanley, H. B. X-ray and neutron scattering from rough surfaces. *Phys. Rev. B* **38**, 2297–2311 (1988). 1, 14, 17, 55, 62

[7] Holy´, V., Kubeˇna, J., Ohli´dal, I., Lischka, K. & Plotz, W. X-ray reflection from rough layered systems. *Phys. Rev. B* **47**, 15896–15903 (1993). 1, 23, 46, 55

[8] Pedrotti, F. L., Pedrotti, L. M. & Pedrotti, L. S. *Introduction to Optics* (Pearson, 2007), 3. edn. 4, 7, 42

[9] Schiff, L. I. *Quantum Mechanics* (McGraw-Hill, 1968). 6, 59

[10] Popovic, Z. & Popovic, D. B. *Introductory Electromagnetics* (Prentice Hall, 2000). 7, 9

[11] Griffiths, D. J. *Introduction to Electrodynamics.* (Pearson, 2008), 3. edn. 9

[12] Vidal, B. & Vincent, P. Metallic multilayers for x rays using classical thin-film theory. *Appl. Opt.* **23**, 1794–1801 (1984). URL `http://ao.osa.org/abstract.cfm?URI=ao-23-11-1794`. 12

[13] Daillant, J. & Gibaud, A. *X-ray and Neutron Reflectivity.* (Springer, 2009), 1. edn. 18, 22

[14] Ritala, M. & Leskelä, M. *Handbook of Thin Film Materials.* (Academic Press, 2002). 26

[15] Oliphant, T. E. Python for scientific computing. *Computing in Science and Engineering* **9**, 10–20 (2007). 33

[16] Press, H. W., Teukolsky, S. A., Vetterling, W. T. & Flannery, B. P. *Numerical Recipes* (Cambridge University Press, 2007). 34, 36

[17] Jones, E., Oliphant, T., Peterson, P. *et al.* SciPy: Open source scientific tools for Python (2001–). URL `http://www.scipy.org/`. 38

[18] Yoneda, Y. Anomalous surface reflection of x rays. *Phys. Rev.* **131**, 2010–2013 (1963). 41

[19] Henke, B. L., Gullikson, E. M. & Davis, J. C. X-ray interactions: Photoabsorption, scattering, transmission, and reflection at e = 50-30,000 ev, z = 1-92. *Atomic Data and Nuclear Data Tables* **54**, 181 – 342 (1993). URL `http://www.sciencedirect.com/science/article/pii/S0092640X83710132`. 46

[20] Björck, M. & Andersson, G. *GenX*: an extensible X-ray reflectivity refinement program utilizing differential evolution. *Journal of Applied Crystallography* **40**, 1174–1178 (2007). URL `http://dx.doi.org/10.1107/S0021889807045086`. 46, 55

[21] Frigo, M. & Johnson, S. The design and implementation of fftw3. *Proceedings of the IEEE* **93**, 216 –231 (2005). 54

[22] Govindaraju, N. K., Lloyd, B., Dotsenko, Y., Smith, B. & Manferdelli, J. High performance discrete fourier transforms on graphics processors. In *Proceedings of the 2008 ACM/IEEE conference on Supercomputing*, SC ’08, 2:1–2:12 (IEEE Press, Piscataway, NJ, USA, 2008). URL `http://portal.acm.org/citation.cfm?id=1413370.1413373`. 54

[23] Moreland, K. & Angel, E. The fft on a gpu. In *Proceedings of the ACM SIGGRAPH/EUROGRAPHICS conference on Graphics hardware*, HWWS ’03, 112–119 (Eurographics Association, Aire-la-Ville, Switzerland, Switzerland, 2003). URL `http://portal.acm.org/citation.cfm?id=844174.844191`. 54

[24] Cooley, J. W. & Tukey, J. W. An algorithm for the machine calculation of complex Fourier series. *Math. Comp.* **19**, 297–301 (1965). 63

Appendix A

DWBA - General Expression

This chapter offers a brief overview of the derivation of the general expression for the BA and the DWBA. It is assumed that the reader has some basic knowledge of quantum mechanics. The derivation follows the steps given by Schiff in [9].

The wave function $\Psi(\mathbf{r},t)$ of a particle with mass m in all places $\mathbf{r}$ at a time t, described by the full Schrödinger equation,

$$i\hbar\frac{\partial}{\partial t}\Psi(\mathbf{r},t) = \left(-\frac{\hbar^2}{2m}\nabla^2 + V(\mathbf{r},t)\right)\Psi(\mathbf{r},t) \tag{A.1}$$

contains *all* information about the particle. This includes the wave function at some later time t' and place r', which can be written explicitly as

$$\Psi(\mathbf{r}',t') = i\int G(\mathbf{r}',t';\mathbf{r},t)\Psi(\mathbf{r},t)\ \mathrm{d}^3r, \tag{A.2}$$

where G is the *Green's function*. Here, this function acts as a *propagator* describing the probability amplitude of going from the state $\Psi(\mathbf{r},t)$ to $\Psi(\mathbf{r}',t')$, given $t < t'$. That is, G can be used to describe the wave function $\Psi(\mathbf{r},t)$ at a different point in time.

Consider an initially free particle ($V = 0$) with wave function $\Phi_\alpha(\mathbf{r},t)$ incident on a potential ($V \neq 0$). Associated with $\Phi_\alpha(\mathbf{r},t)$ is a new wave function $\Psi_\alpha(\mathbf{r},t)$ growing out of $\Phi_\alpha(\mathbf{r},t)$ when the particle enters the potential. Using the Green's propagator, $\Psi_\alpha(\mathbf{r}',t')$ can at some later time ($t < t'$) be expressed as

$$\Psi_\alpha(\mathbf{r}',t') = i\int G(\mathbf{r}',t';\mathbf{r},t)\Phi_\alpha(\mathbf{r},t)\ \mathrm{d}^3r. \tag{A.3}$$

At some time in the future, t', the particle will have left the potential, and $\Psi_\alpha(\mathbf{r}',t')$ will necessarily be a solution of the free particle Schrödinger equation. The probability amplitude of the (scattered) free particle state $\Phi_\beta(\mathbf{r}',t')$ contained in $\Psi_\alpha(\mathbf{r}',t')$ is then defined as the quantity

$$\langle\beta|S|\alpha\rangle \equiv \langle\Phi_\beta|\Psi_\alpha\rangle\,, \tag{A.4}$$

where S is the unitary *scattering matrix* or S *matrix*. The scattering matrix relates the initial state and final states of a scattering process. Φ_α and Φ_β represent an incoming and a scattered outgoing wave, cf. fig. A.1. Substituting eq. (A.3) we get

$$\langle\beta|S|\alpha\rangle = i \iint \Phi^*_\beta(\mathbf{r}', t') G(\mathbf{r}', t'; \mathbf{r}, t) \Phi_\alpha(\mathbf{r}, t) \, \mathrm{d}^3r' \, \mathrm{d}^3r, \tag{A.5}$$

which can be rewritten as

$$\langle\beta|S|\alpha\rangle = \langle\beta|\alpha\rangle - \frac{i}{\hbar} \iint \Phi^*_\beta(\mathbf{r}, t) V(\mathbf{r}, t) \Psi_\alpha(\mathbf{r}, t) \, \mathrm{d}t \, \mathrm{d}^3r \tag{A.6}$$

where $\langle\beta|\alpha\rangle \equiv \int \Phi^*_\beta(\mathbf{r}, t)\Psi_\alpha(\mathbf{r}, t) \, \mathrm{d}^3r$.

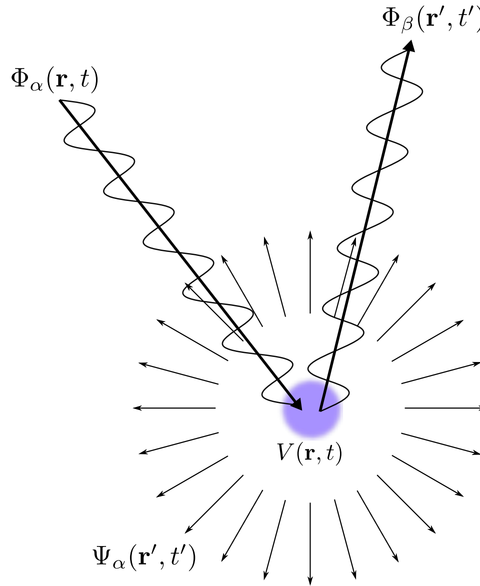

Figure A.1: A free particle described by $\Phi_\alpha(\mathbf{r}, t)$ strikes the potential $V(\mathbf{r}, t)$, giving rise to a spherical wave $\Psi_\alpha(\mathbf{r}', t')$. The probability amplitude of the (scattered) free particle state $\Phi_\beta(\mathbf{r}', t')$ contained in $\Psi_\alpha(\mathbf{r}', t')$ is given by eq. (A.4).

The above theory allows for the potential V to vary in time beyond just being switched on and then off at a later time. In stationary scattering theory, however, the potential is constant in an interval between being switched on and off, which allows for some simplifications (imagine a particle entering and leaving a constant potential, corresponding to switching the potential on, and then off). In such cases it is more convenient to deal with transition probability amplitude per unit of time. This assumption of a stationary potential (i.e. not varying in time) is valid for most interactions of X-rays with matter.

Consider a situation where

$$\Phi_\alpha(\mathbf{r},t) = u_\alpha(\mathbf{r})e^{-i\omega_\alpha t} \qquad\qquad V = 0 \tag{A.7}$$

$$\Psi_\alpha(\mathbf{r},t) = \chi_\alpha(\mathbf{r})e^{-i\omega_\alpha t} \qquad\qquad V(\mathbf{r},t) = V(\mathbf{r})g(t) \tag{A.8}$$

The time dependence of the potential $V(\mathbf{r},t)$ is determined by $g(t)$, which is equal to one during the time span Δt when the particle is in the potential. The *transition matrix* or *T matrix* is defined through

$$\langle\beta|S-1|\alpha\rangle = -\frac{i}{\hbar}\langle\beta|T|\alpha\rangle \int_{-\infty}^{\infty} g(t)e^{i(\omega_\beta-\omega_\alpha)t}\,\mathrm{d}t, \tag{A.9}$$

where

$$\langle\beta|T|\alpha\rangle \equiv \int u_\beta^*(\mathbf{r})V(\mathbf{r})\chi_\alpha(\mathbf{r})\,\mathrm{d}^3r. \tag{A.10}$$

In contrast to the S-matrix, the T-matrix has no time dependency. For situations where $\Delta t \to \infty$ (a stationary system) it is not meaningful to think in terms of a transition probability. We use instead the scattering amplitude, which is given by

$$f(\mathbf{k}_\beta,\mathbf{k}_\alpha) = -\frac{m}{2\pi\hbar^2|C|^2}\langle\beta|T|\alpha\rangle\,, \tag{A.11}$$

where m is the particle mass. Here we have used that

$$u_\alpha = Ce^{i\mathbf{k}_\alpha\cdot\mathbf{r}} \tag{A.12}$$

$$u_\beta = Ce^{i\mathbf{k}_\beta\cdot\mathbf{r}}, \tag{A.13}$$

where $\mathbf{k}_\beta$ and $\mathbf{k}_\alpha$ are wave vectors and C is a normalization constant. The differential scattering cross section, which describes the probability of finding a scattered particle within a given solid angle, is given by

$$\frac{\mathrm{d}\sigma}{\mathrm{d}\Omega} = |f(\mathbf{k}_\beta,\mathbf{k}_\alpha)|^2 = \frac{m^2}{4\pi^2\hbar^4|C|^4}\left|\langle\beta|T|\alpha\rangle\right|^2. \tag{A.14}$$

Equation (A.11) is exact, but not easy to use in practice. In the *Born approximation* we use the property that $\chi_\alpha(\mathbf{r})$ can be written as an infinite perturbation series, which to first order is equal to $u_\alpha(\mathbf{r})$, such that

$$f_{BA}(\mathbf{k}_\beta,\mathbf{k}_\alpha) = -\frac{m}{2\pi\hbar^2|C|^2}\int u_\beta^*(\mathbf{r})V(\mathbf{r})u_\alpha(\mathbf{r})\,\mathrm{d}^3r \tag{A.15}$$

$$= -\frac{m}{2\pi\hbar^2|C|^2}\int V(\mathbf{r})e^{i(\mathbf{k}_\alpha-\mathbf{k}_\beta)\cdot\mathbf{r}}\,\mathrm{d}^3r. \tag{A.16}$$

The approximation of $\chi_\alpha(\mathbf{r})$ to first order might seem drastic, but it should be noted that for a stationary scattering problem, the expected solution for $\chi_\alpha(\mathbf{r})$

has the asymptotic form of a plane wave plus an outgoing spherical wave. The solution should be expressible by

$$\chi_\alpha(\mathbf{r}) = u_\alpha(\mathbf{r}) + Cv(\mathbf{r}) \tag{A.17}$$

where $u_\alpha(\mathbf{r})$ is the plane wave and $v(\mathbf{r})$ is the scattered outgoing spherical wave. As long as $C|v(\mathbf{r})|$ is small in comparison with $|u_\alpha(\mathbf{r})| = C|e^{i\mathbf{k}_\alpha \cdot \mathbf{r}}| = 1$, the first order Born approximation is valid.

Sometimes it is convenient to write the potential as the sum of two parts, $V = V_0 + V_1$, where V_1 is so small that it can be treated as a perturbation. For our purposes, V_0 will be the scattering potential of a perfectly smooth surface, and V_1 a small correction term to the potential to account for possible surface roughness (that will cause diffuse scattering in addition to the specular component). It can be shown that

$$\begin{aligned}
\langle\beta| T |\alpha\rangle &= \langle u_\beta | V_0 + V_1 | \chi_\alpha \rangle \\
&= \left\langle \chi_\beta^- \middle| V_0 + V_1 \middle| u_\alpha \right\rangle \\
&= \left\langle \chi_{0\beta}^- \middle| V_0 \middle| u_\alpha \right\rangle + \left\langle \chi_{0\beta}^- \middle| V_1 \middle| \chi_\alpha \right\rangle
\end{aligned} \tag{A.18}$$

where $\chi_{0\beta}^-$ is equal to the plane wave u_β plus a an ingoing spherical wave describing the scattering due *only* to V_0. In contrast, χ_α is equal to the plane wave u_α plus an outgoing spherical wave describing the scattering from *both* V_0 and V_1. It might seem strange that the final state $\chi_{0\beta}^-$ is associated with an *ingoing* spherical wave, but it is the only viable solution as an outgoing spherical state would necessarily contribute to the scattering amplitudes in other directions.

Equation (A.18) is exact. If, however, we replace χ_α by $\chi_{0\alpha}$, the T-matrix element in the *distorted-wave Born approximation* is obtained:

$$\boxed{\langle\beta| T |\alpha\rangle = \left\langle \chi_{0\beta}^- \middle| V_0 \middle| u_\alpha \right\rangle + \left\langle \chi_{0\beta}^- \middle| V_1 \middle| \chi_{0\alpha} \right\rangle} \tag{A.19}$$

Although we began this section with the Schrödinger equation of a particle with finite mass, the theory is also valid for mass-less X-ray photons of wavelength λ. X-rays obey the stationary wave equation [6]

$$\nabla^2\psi + k_0^2\psi - V\psi = 0, \tag{A.20}$$

where $V = k_0^2(1 - n^2)$, $k_0 \equiv 2\pi/\lambda$ is the magnitude of the wave vector, and n is the refractive index of the medium.

Appendix B

Fast Fourier Transform

This appendix extends upon section 5.1.1.

The frequency spectrum resulting from any DFT is *even* around ω_0 such that $F(\omega_n) = F(\omega_{n+N/2})$, so there is evidently some redundancy in the calculations. Furthermore, the sum in the DFT function can be rearranged into an even indexed and an odd-indexed part:

$$\underbrace{\sum_{j=0}^{N-1} f_j e^{\frac{2\pi i}{N} nj}}_{\text{DFT - } all \text{ indices}} = \underbrace{\sum_{j=0}^{N/2-1} f_{2j} e^{\frac{2\pi i}{N/2} nj}}_{\text{DFT - } even \text{ indices}} + e^{\frac{2\pi i}{N} n} \underbrace{\sum_{j=0}^{N/2-1} f_{2j+1} e^{\frac{2\pi i}{N/2} nj}}_{\text{DFT - } odd \text{ indices}} \tag{B.1}$$

$$= F^e(\omega_n) + wF^o(\omega_n) \tag{B.2}$$

This can be done $\log_2(N)$ times until the there is only one h left for each DFT. Recall now that only half of the $F(\omega_n)$'s have to be calculated for each DFT due to redundancy. Since we have split the original DFT $\log_2(N)$ times as demonstrated in eq. (B.2), the pivotal result is that we only need to compute $F(\omega_0 = 0)$, although for N DFTs (each with one f). The concept is clarified in fig. B.1. The consequence is a dramatic reduction in the number of computational operations, which is now proportional to $N \log_2(N)$. The method described above is called the FFT algorithm, and it was discovered in 1805 by Carl Friedrich Gauss and rediscovered and popularized in 1965 by J. W. Cooley and John W. Tukey [24].

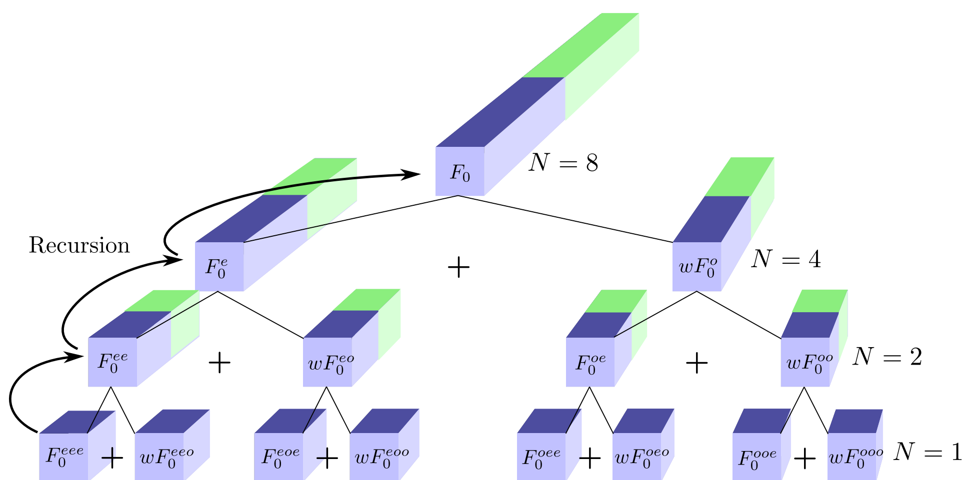

Figure B.1: The number of computational operations required for a fast Fourier transform (FFT) is proportional to $N \log_2 N$, whereas the number required by the naive approach is proportional to N^2. The figure demonstrates the basic intuition behind an FFT of size $N = 8$. That is, eight different frequencies and thus eight F_n and eight f_j's: The topmost array holds the DFTs corresponding to all eight F_n's, half of which come "for free" due to symmetry (green color). The remaining F_n's are split in separate DFTs for odd and even indices. Again, for the new DFTs, half of the F_n's come for free. The latter procedure is repeated $log_2 N = 3$ times until there only remaining frequency is F_0, and each of the $N = 8$ DFTs are functions of *one* f. The resulting number of computations is therefore equal to $N \log_2 N$. The procedure is most easily carried out recursively.